

TRANSIENT ANALYSIS OF ELECTRONS
DRIFTING IN LIQUID ARGON

by

Paul Robert Schenk

B.Sc., University of Western Ontario, 1987

ACCEPTED
FACULTY OF GRADUATE STUDIES

DATE

April 18, 1989

DEAN

A THESIS SUBMITTED IN PARTIAL FULFILLMENT
OF THE REQUIREMENTS FOR THE DEGREE OF
MASTER OF SCIENCE

in the Department
of
Physics

We accept this thesis as conforming to the required standard

Supervisor Dr. R.K. Keeler

Dr. A. Astbury

Dr. L.P. Robertson

Dr. D.A. Harrington

Dr. D. Hanna


©PAUL ROBERT SCHENK, 1989
University of Victoria

*All rights reserved. This thesis may not be reproduced
in whole or in part, by mimeograph or other means,
without the permission of the author.*

Supervisor: Professor Richard K. Keeler

ABSTRACT We have produced purified liquid argon and have analysed pulses produced by cosmic ray muons in a parallel plate ionisation chamber by transient pulse shape analysis. Our measured electron lifetime of $(95.1^{+7.1}_{-6.9} \pm 43)\mu s$ corresponds to an impurity concentration of $2.36\text{ppb } O_2$ equivalent at $30V/cm$ applied field. The low field electron mobility is measured to be $(451 \pm 1 \pm 68)cm^2/Vs$ at $90^\circ k$. We measure the free ion yield per 100eV to be $3.2^{+0.2}_{-0.6}$.


Examiners:


Supervisor Dr. R.K. Keeler


Dr. A. Astbury


Dr. L.P. Robertson


Dr. D.A. Harrington


Dr. D. Hanna

Contents

Abstract	ii
Contents	iii
List of Tables	v
List of Figures	vi
Acknowledgement	ix
1 Introduction	1
2 Chapter Two	3
2.1 The nature of signals from drift cells	3
2.2 Electron Mobility in LAr	12
2.3 Cosmic Ray Muons	15
3 Apparatus	19
3.1 Cryogenics System	19
3.2 Sieve vessel and preparation	24
3.3 Cell vessel and preparation	26
3.4 Argon Purification	30
3.5 Data Acquisition System	30
3.6 Data Taking	33
4 Data Analysis	36
4.1 Initial Data Selection	36
4.2 Determination of the drift velocity and the electron lifetime . .	42

4.3	Determination of the Absolute Charge Yield	54
5	Conclusion	60
	Bibliography	61
A	Transfer function and Pulse shape	63

List of Tables

- 1 The number of pulses taken at each voltage and the conditions 33
- 2 The number of pulses at each voltage that pass the cuts 42
- 3 The fits for the drift time and lifetime for the voltages. The errors are the statistical errors in the fit. 45

List of Figures

1	A parallel plate ion chamber and the associated readout circuit. The chamber is traversed by a charged track parallel to the applied field.	5
2	Two electrically connected conducting sheets with an insulating charged sheet between them	5
3	A line of positive charges growing towards $x = 0$	6
4	The free ion yield in LAr per 100eV energy absorbed. From [3]	10
5	The electron attachment rate constants for SF_6 , N_2O and O_2 as a function of field. [7]	11
6	The electron drift velocity in LAr as a function of field. From [9]	13
7	Electron Mobility in LAr as a function of temperature. [9] . .	14
8	The cosmic ray muon intensity as a function of momentum at sea level. [10]	15
9	The Vavilov distribution for $\kappa = 0.438$ and $\beta = 0.969$. The bin size is 0.09 in λ	18
10	Schematic diagram of the LAr purification and test apparatus	20
11	Schematic cross section of the LN_2 Vessel	21
12	LN_2 Vapour pressure vs. temperature	22
13	A schematic of the LN_2 level controller. The sensor resistors are composite carbon.	23
14	The liquid nitrogen transfer system	24
15	Schematic cross section of the sieve vessel	25
16	Schematic cross section of the LAr cell	27

17	Residual gas in the system before filling	28
18	The lines of constant potential obtained with a 0.5mm grid.	29
19	The data readout chain and the high voltage input.	31
20	The transfer function at $\times 4$ gain normalized to 10^4 electrons input, with the fit superimposed. The bottom picture is an expansion of the top.	34
21	The transfer function at $\times 6$ gain normalized to 10^4 electrons input, with the fit superimposed. The bottom picture is an expansion of the top.	35
22	A typical pulse as digitized by the transient analyzer	37
23	The integral of the pulse rise vs. the pulse height. The points inside the box make the cuts on these two variables.	39
24	The χ^2 of the fit to a flat peak. The arrow shows where the cut was made.	40
25	TOP: The pulse height spectrum with the two pulse height cuts. BOTTOM: The same with the χ^2 cut.	41
26	A sample average obtained. Notice that the tail falls below zero.	43
27	The χ^2 of the pulse fit vs. the number of points in the fit. The pulse peaks at 1300 and the transfer function cutoff is at 2100.	46
28	The averaged pulse at 1000 V/cm with the fit superimposed.	47
29	The averaged pulse at 400 V/cm with the fit superimposed.	48
30	The averaged pulse at 333 V/cm with the fit superimposed.	49
31	The averaged pulse at 200 V/cm with the fit superimposed.	50
32	The averaged pulse at 100 V/cm with the fit superimposed.	51
33	The averaged pulse at 40 V/cm with the fit superimposed.	52

34	The averaged pulse at 30 V/cm with the fit superimposed. . .	53
35	The Drift velocity vs. Electric field for our LAr sample. The line corresponds to $\mu_e = 451 \text{ cm}^2/\text{Vs}$	55
36	A typical free electron yield spectrum.	57
37	The random energy deposited in the cell.	58
38	The free ion yield per 100 eV in our LAr sample. The line is from the data of reference [23].	59
39	The equivalent circuit for an amplification chain.	64
40	The pre-amp approximated by a single integrator.	64

Acknowledgement

There are many people who have helped make this project a reality. First I owe many thanks to W. James Slater, whose help with the myriad of tasks needed to get signals from our LAr cell was indispensable. I'd also like to thank Dave Smith and Peter Verstraaten for machining and welding the apparatus and Ted Gathright for the original cell chamber design.

I am grateful to Sean Beingessner, Margret Fincke-Keeler, Paul Poffenberger, Myron Rosvick and Andre Turcot, who made sure things kept running during my absences.

I also would like to thank Mike Shepherd for his advice on L^AT_EX, AWK and countless other topics and Roy Langstaff for his drawings of the apparatus. I thank Rita d'Entremont for typing the thesis, digitizing many of the figures and being there when things looked bleak.

Finally I'd like to thank Richard Keeler for his continued guidance and support.

1 Introduction

Liquid argon (LAr) has been used as the active medium in total absorption detectors for high energy physics since Radeka and Willis built their first test chamber in 1974 [1]. As an active calorimeter medium LAr has many advantages: It is dense in comparison to other common media ($1.4g/cm^3$ as compared to $2.67 \times 10^{-3}g/cm^3$ for Isobutane at STP and $1.03g/cm^3$ for Polystyrene). Argon is not electronegative and thus non-ionised molecules will not degrade the signal by attaching electrons. Electrons in LAr can have high drift velocities ($5mm/\mu s$ @ $1kV/mm$), thus allowing for fast signal collection. LAr is resistant to radiation damage, thus allowing a detector to operate at a fairly constant gain for its entire lifetime and in a high radiation environment. This is in contrast to scintillators which are prone to radiation damage.

LAr also offers the possibility of good energy resolution as the average energy to create an electron ion pair is about $23.6eV$ [2] and the theoretical minimum energy resolution is $5.19KeV(fwhm)$ for a $1MeV$ photon [3]. This rivals $Ge(Li)$ detectors which achieve a $1.5keV(fwhm)$ resolution under the same conditions. While the resolution can theoretically be this low, no detector using LAr has achieved this resolution. In fact, the best resolution stands at $26keV(fwhm)$ for the $976keV$ ^{207}Bi conversion electron. This worse than expected resolution is still a matter of investigation, however even at the achieved resolutions LAr is an attractive active medium for calorimetry.

LAr has another very intriguing property which opens up many possible detector applications. In the limit of perfectly pure argon, electrons

produced in the liquid that escape recombination with their parent ion could drift under the influence of an electric field indefinitely; this is because argon has no affinity for electrons. Now in a real situation there are always impurities, however it is possible to produce LAr pure enough to drift electrons with an attenuation length of $18m @ 1kV/cm$ [4]. With drift lengths on the scale of meters, the possibility of LAr time projection chambers can be considered. These detectors would offer an entirely homogeneous active volume, thus avoiding sampling fluctuations, and fine readout segmentation at a reasonable cost.

We describe here our efforts to purify and measure the purity of liquid argon, using pulse shape analysis of cosmic ray muon tracks in a parallel plate chamber. The drift velocity and ion yield will also be measured and compared with previous experiments.

2 Chapter Two

2.1 The nature of signals from drift cells

We now investigate the signal shape from an ionisation chamber due to the passage of a charged particle. The signal will be a transient voltage measured at AA' due to the separation of the electron-ion pairs left by the passage of an ionising particle as shown in figure 1.

To proceed we must first find the charge induced on a parallel plate capacitor by a single charge. Consider two infinite conducting plates, electrically connected with a nonconducting sheet of surface charge density σ between them (see figure 2). Since the plates are electrically connected, the potential difference between $x = 0$ and $x = d$ is zero.

What we want to know is the charge density on the plate at $x = 0$ (denoted σ') as a function of a , the distance between the plate and the charged sheet. If we call σ'' the charge density at $x = d$ we can see from Gauss' law that

$$\sigma' + \sigma'' = -\sigma \quad (1)$$

by considering the surface S in figure 2.

The potential inside the space due the plate at $x = 0$ is

$$\phi_0(x) = \frac{-\sigma'x}{2\epsilon_0} \quad (2)$$

and due to the plate at $x=d$ the potential is

$$\phi_d(x) = \frac{\sigma''(x-d)}{2\epsilon_0} \quad (3)$$

Due to the charged sheet the potential is

$$\phi_{sheet}(x) = \begin{cases} \frac{\sigma(x-a)}{2\epsilon_0} & x \leq a \\ \frac{\sigma(a-x)}{2\epsilon_0} & x > a \end{cases} \quad (4)$$

Since the plates are connected electrically

$$\Delta\phi|_0^d = \phi(d) - \phi(0) = 0 \quad (5)$$

Using (2), (3) and (4) we have,

$$\phi(0) = \frac{-1}{2\epsilon_0} [d\sigma'' + a\sigma] \quad (6)$$

and

$$\phi(d) = \frac{1}{2\epsilon_0} [-d\sigma' + (a-d)\sigma] \quad (7)$$

Equations (5), (6) and (7) give us that,

$$\sigma' - \sigma'' = \frac{\sigma(2a-d)}{d} \quad (8)$$

Using 1 to eliminate σ'' finally gives us that

$$\sigma' = -\sigma \left(1 - \frac{a}{d} \right) \quad (9)$$

(We have ignored any effect due to the outside plate surfaces, since any such effect would create an unphysical dependence on the width of the plates.)

What we are interested in however, is an electron (charge $-e$) between the two plates. First we note that $q' + q'' = +e$ from (1). By the

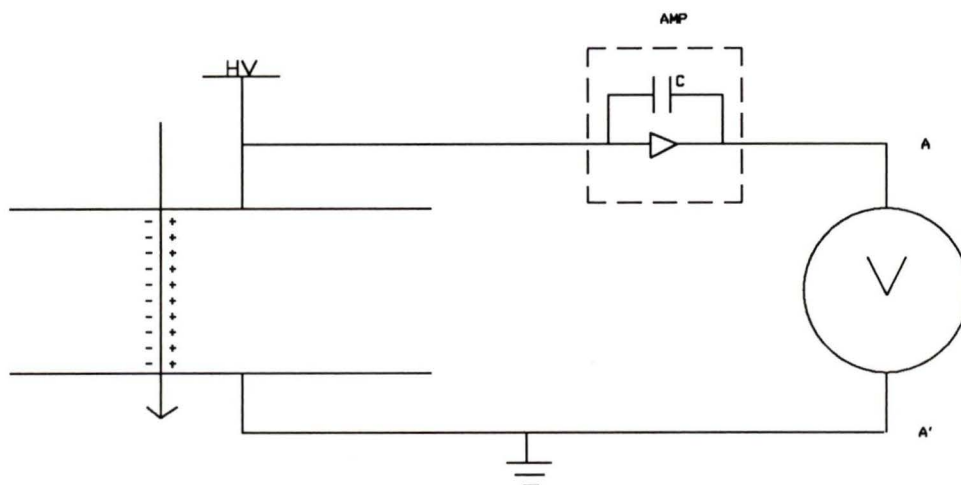


Figure 1: A parallel plate ion chamber and the associated readout circuit. The chamber is traversed by a charged track parallel to the applied field.

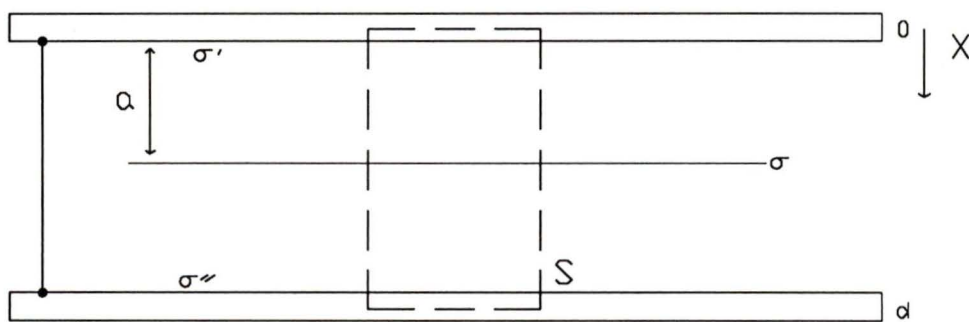


Figure 2: Two electrically connected conducting sheets with an insulating charged sheet between them

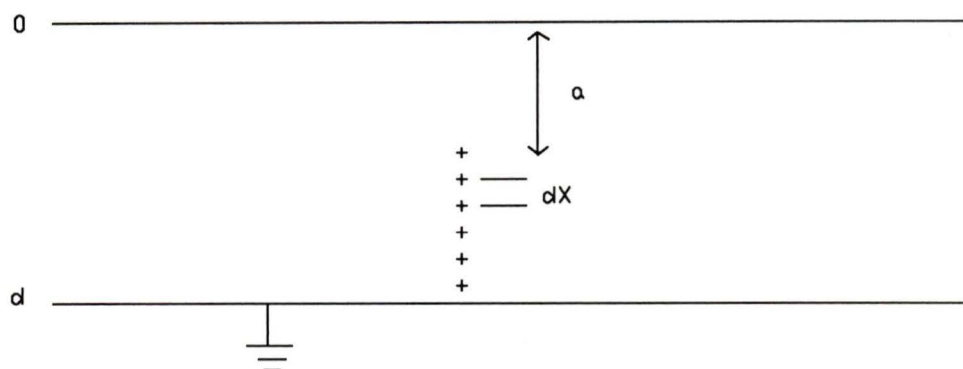


Figure 3: A line of positive charges growing towards $x = 0$

superposition principle, if we place another electron anywhere on the plane $x = a$, we would just have $q' + q'' = +2e$ and so on. That is, the induced charge q' would be the same for an individual electron as if the same charge was smeared over a sheet. Thus for the plate at $x = 0$

$$q' = e \left[1 - \frac{x}{d} \right] \quad (10)$$

is the charge induced by an electron at x .

Now we consider the signal at AA' produced by the electrons drifting away from their parent ions. (The positive ions have mobilities many times smaller than the electrons and hence may be assumed stationary). The electrons will drift along the field (at a velocity v_d) leaving behind a trail of positively charged ions. This situation is equivalent to a line of positive ions growing from $x = d$ towards $x = 0$ at the rate v_d (figure 3) and electrons being deposited at $x = 0$ at the rate $\frac{N}{d}v_d$ (N is the total number of free pairs in the track).

The induced charge at $x = 0$ due to a positive ion at x is, from (10)

$$q_{ind} = -e \left[1 - \frac{x}{d} \right] \quad (11)$$

Letting $\lambda = \frac{Ne}{d}$ we can write the induced charge by a small portion of a line of positive charge as

$$dq_{ind} = -\lambda \left[1 - \frac{x}{d} \right] dx \quad (12)$$

Integrating (12) to find the charge induced by a column of positive ions between a and d yields

$$q_{ind}(a) = -\lambda \left[\frac{d}{2} - a + \frac{a^2}{2d} \right] \quad (13)$$

We note that $a = a(t) = d - v_d t$ thus (13) becomes

$$q_{ind}(t) = -\lambda \frac{v_d^2 t^2}{2d} \quad (14)$$

This induced charge at $x = 0$ arises from two sources. One is the electrons being absorbed by the plate

$$q_{abs}(t) = -\lambda v_d t \quad (15)$$

and the rest of the charge comes from the current flowing in the circuit connecting the two plates q_{curr} . We have then

$$q_{ind}(t) = q_{abs}(t) + q_{curr}(t) \quad (16)$$

Equations (14) , (15) and (16) give us that the charge flowing in the external circuit is

$$q_{curr}(t) = Ne \frac{t}{\tau_d} \left[1 - \frac{t}{2\tau_d} \right] \quad (17)$$

where we have introduced τ_d , the time for an electron to drift the entire distance between the plates ($\tau_d = \frac{d}{v_d}$). These flowing charges give rise to a current in the circuit

$$I_{sig}(t) = \frac{dq_{curr}}{dt} = \begin{cases} 0 & t < 0 \\ \frac{Ne}{\tau_d} \left[1 - \frac{t}{\tau_d} \right] & 0 < t \leq \tau_d \\ 0 & t > \tau_d \end{cases} \quad (18)$$

this is the detectable signal in our circuit in figure 1. We note also that this is the current due to the electrons flowing in the gap.

The amplifier in figure 1 integrates the current on the capacitor C and thus presents a voltage at AA' . If the amplifier was a perfect integrator we would have

$$V_{AA}(t) = \frac{1}{C} \int_0^t I_{sig}(t') dt' = \begin{cases} \frac{Ne}{C\tau_d} \left[t - \frac{t^2}{2\tau_d} \right] & t \leq \tau_d \\ \frac{Ne}{2C} & t > \tau_d \end{cases} \quad (19)$$

This expression shows that for $t > \tau_d$ the total detected charge is that of only one half of the total electrons available. The "missing half" will be detected after the positive ions have all drifted to the grounded plate.

Real amplifiers are not perfect integrators however and thus (19) is modified to be

$$V_{AA'}(t) = \int_0^t h(t-x) I_{sig}(x) dx \quad (20)$$

where $h(t)$ is the transfer function of the amplifier (see Appendix A).

There are two processes that work to change the expected pulse height and shape given in (20). One is initial (or germinate) recombination and the other is electron capture.

Germinate recombination is the recombination of an electron with its parent ion before the electron has had time to drift and create a signal. This process changes N , the number of ions. The free electron yield (i.e. the number of electrons escaping initial recombination) as a function of the applied electric field is generally taken to be given by the Onsager model [5]. This model gives the number of free electrons N as a function of field as [4],

$$N(E) = N_0(1 + \alpha E) \quad (21)$$

with N_0 , the number of free electrons obtained at zero field. In (21)

$$\alpha = \frac{er_c}{2k_B T} \quad (22)$$

and r_c is called the critical Onsager radius given by

$$r_c = \frac{e^2}{4\pi\epsilon k_B T} \quad (23)$$

This linear variation of yield with field seems to hold for low fields, but is not the case for high fields as can be seen in figure 4.

The other process affects the actual pulse shape. This process is electron capture, which is the trapping of electrons by electronegative molecules such as O_2 , i.e.:



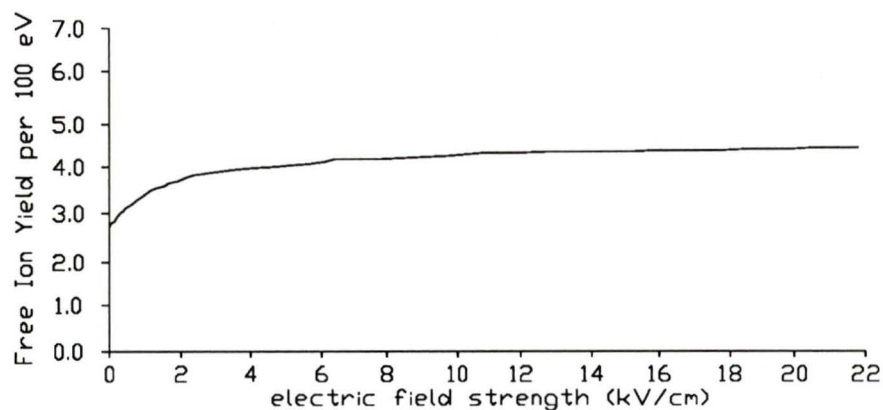


Figure 4: The free ion yield in LAr per 100eV energy absorbed. From [3]

This results in a negatively charged ion, which will have a mobility comparable to the Ar^+ ions and hence are effectively stationary. As the electrons drift towards the collecting plate, some will be trapped by this reaction thus reducing the signal.

The reaction in (24) traps electrons at the rate

$$k = k_x[X] \quad (25)$$

with k being the trapping rate, k_x the molar rate constant for the reaction in (24) and $[X]$, the molar concentration of X in the liquid. The number of free drifting electrons is given by the equation

$$N(t) = N_0 e^{-kt} \quad (26)$$

We see that $\tau \equiv 1/k$ is the time needed for $1/e$ of the original electrons to be trapped. We call τ the electron lifetime. For more than one species X , we would have

$$\tau = \frac{1}{\sum_i [i] k_i} \quad (27)$$

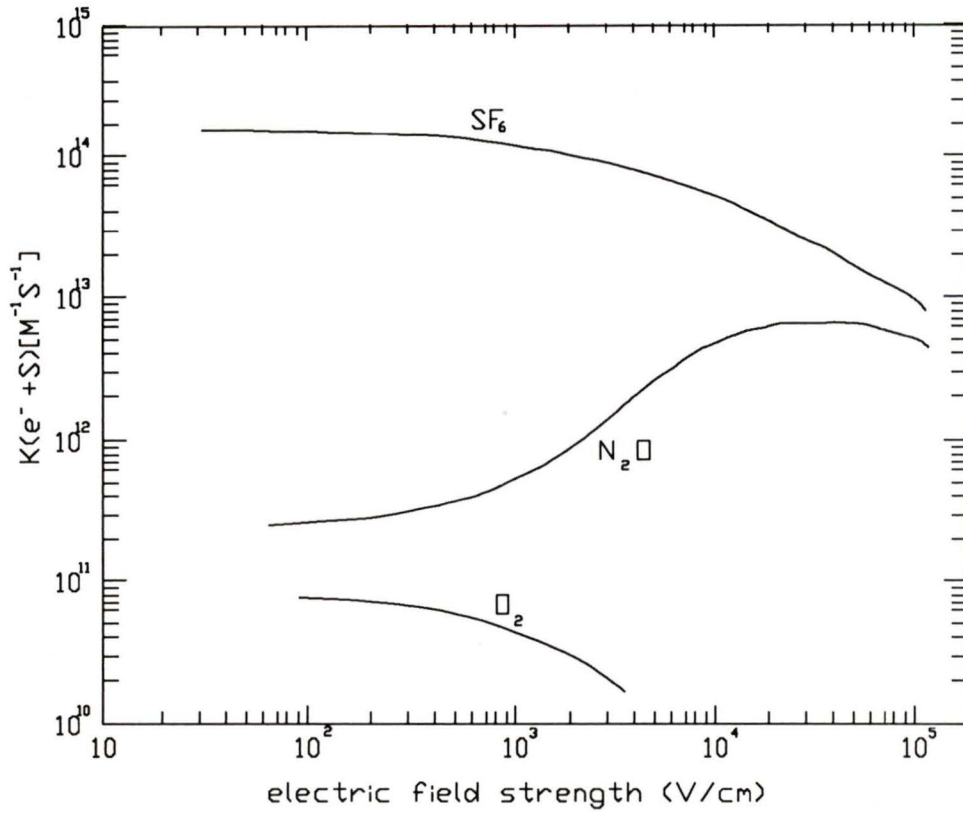


Figure 5: The electron attachment rate constants for SF_6 , N_2O and O_2 as a function of field. [7]

k_i as a function of field for three substances (SF_6 , N_2O and O_2) is shown in figure 5. As it is not usual to know the individual electronegative species present (or their concentrations), the electron lifetime is usually used to state the concentration of oxygen molecules that would give the same lifetime. Such statements are only valid at the given electric field, as the various k_i are functions of E . For O_2 it has been shown that the relation

$$[O_2](ppm) = \frac{0.15E(\frac{kV}{cm})}{\lambda(cm)} \quad (28)$$

holds [6]. Here $\lambda \equiv v_d\tau$, which is the electron attenuation length.

We now investigate the effect of electron attachment on the expected signal given in (18) and (20). First, note that as $\tau \rightarrow \infty$ in (26) $N(t) \rightarrow N_0$. Thus as the lifetime goes to infinity we must recover our original (no attachment) signal. As individual electrons stop flowing in the gap, the current in the circuit will be diminished, thus we expect (18) to be modified to

$$I_{sig}(t) = \frac{dq_{curr}}{dt} = \begin{cases} \frac{Ne}{\tau_d} e^{(-t/\tau)} \left[1 - \frac{t}{\tau_d}\right] & t \leq \tau_d \\ 0 & t > \tau_d \end{cases} \quad (29)$$

We note that as $\tau \rightarrow \infty$ in (26), we do recover (18) and (19). Thus the voltage across AA' in our circuit will be given by (20), with

$$I_{sig}(t) = \begin{cases} \frac{eN_0(E)}{\tau_d(E)} e^{(-t/\tau(E))} \left[1 - \frac{t}{\tau_d(E)}\right] & t \leq \tau_d \\ 0 & t > \tau_d \end{cases} \quad (30)$$

where we have included the implicit field dependence in the various terms.

2.2 Electron Mobility in LAr

The electron mobility is defined by the expression

$$v_d = \mu_e E \quad (31)$$

The mobility of electrons in liquid argon is approximately constant for fields below $300V/cm$, and then falls fairly sharply at higher voltages (see figure 6). The low field mobility in argon is $475cm^2/Vs$ at $85K$ [8], and decreases with increasing temperature until $125K$ (figure 7). We note that this mobility variation with temperature amounts to about 20% between $85K$ and $95K$.

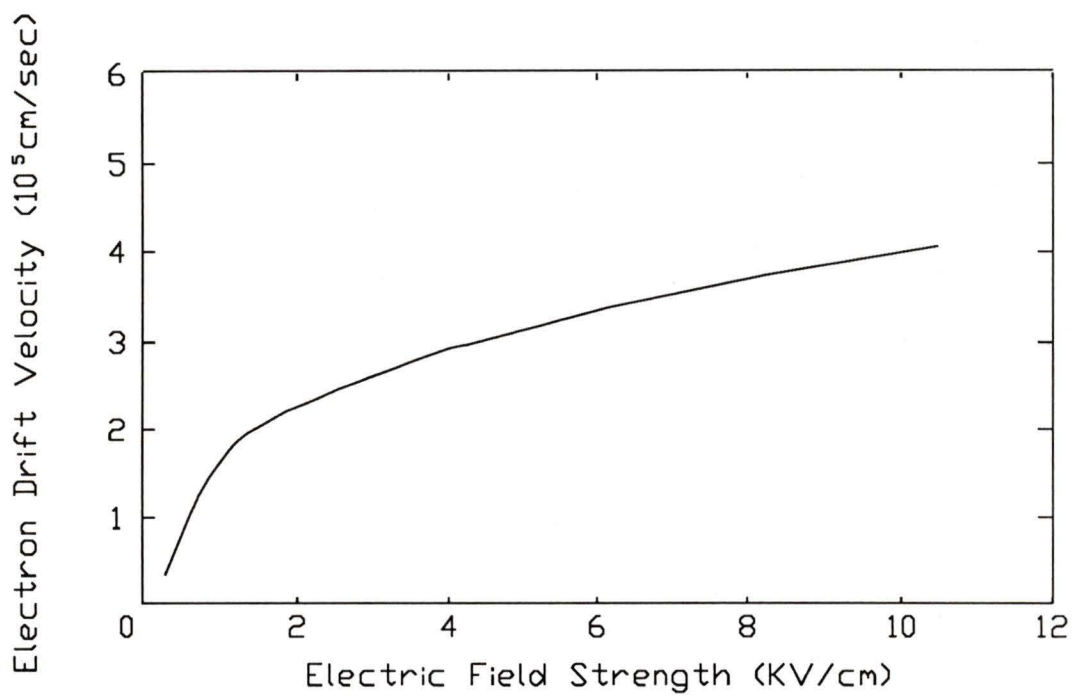


Figure 6: The electron drift velocity in LAr as a function of field. From [9]

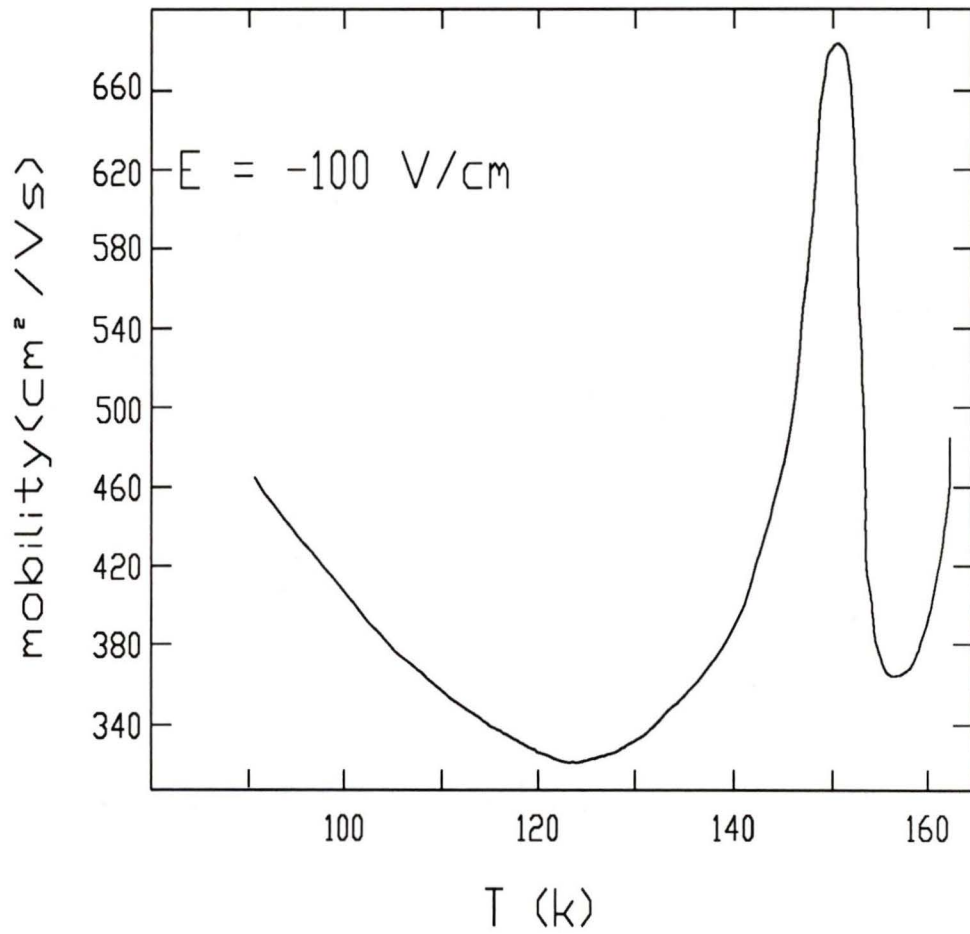


Figure 7: Electron Mobility in LAr as a function of temperature. [9]

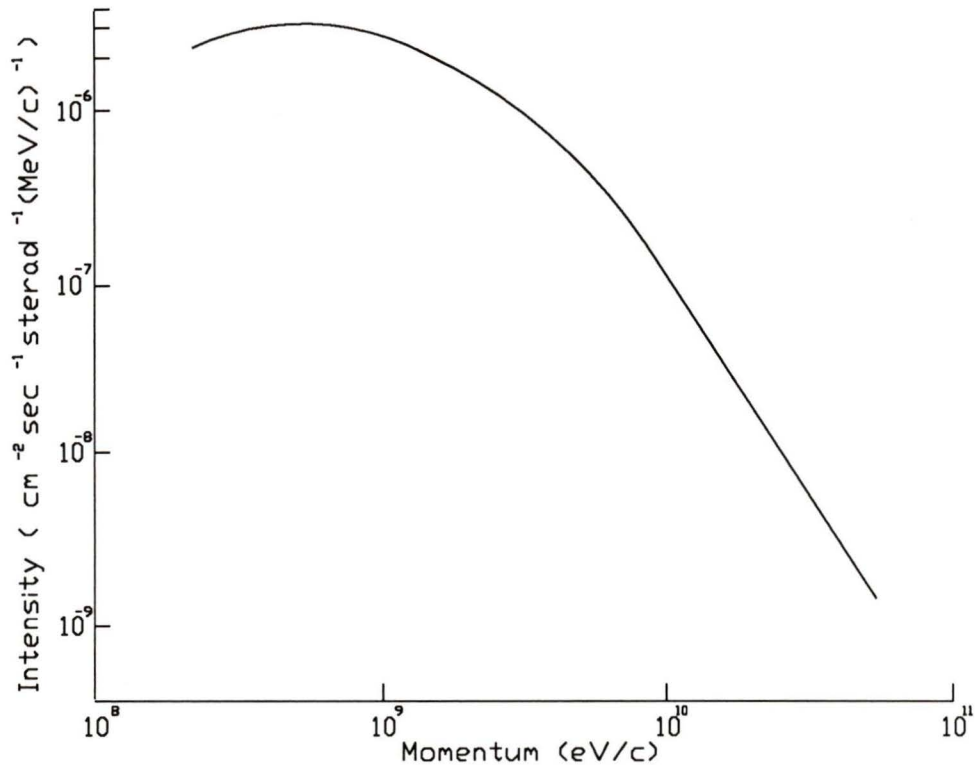


Figure 8: The cosmic ray muon intensity as a function of momentum at sea level. [10]

2.3 Cosmic Ray Muons

The vast majority of cosmic ray particles are muons [10]. These muons arise mostly from pion and kaon decays in the upper atmosphere. The cosmic ray muon flux at sea level in the vertical direction is typically $0.8 \times 10^2 m^2 s^{-1} sterad^{-1}$ with an angular dependence of roughly $\cos^2 \theta$ [11]. The energy spectrum is shown in figure 8. Above momenta of roughly $1 GeV/c$ the intensity of the muons falls nearly as p^{-2} .

As the cosmic ray muons pass through matter, their dominant energy loss mechanism is ionisation. The average energy lost by the muons per unit

path length is well known for various materials and is given by the Bethe-Bloch formula.

$$\frac{dE}{dX} = 4\pi N_A r_e^2 m_e c^2 \frac{Z_{med} \rho_{med}}{A_{med}} \left[\frac{Z_{inc}}{\beta} \right]^2 \left[\ln \left(\frac{2m_e \gamma^2 \beta^2 c^2}{I} \right) - \beta^2 \right] \quad (32)$$

Where N_A is Avagadro's number, r_e is the classical radius of the electron. Z_{med} is the nuclear charge number of the medium (18 for LAr), A_{med} is the mass number of the medium (40 for LAr) and ρ_{med} is the density ($1.4g/cm^3$ for LAr). I characterizes the electron binding energy in the medium and is given approximately by [12]

$$I(eV) \approx [9.76 + 5.88Z^{-1.19}]Z \quad (33)$$

This works out to be $1.79 \times 10^{-4} MeV$ for LAr.

For our purposes it is not only important to know the average energy deposition, but also the fluctuations about this average. This problem was solved by Landau [13] for thin absorbers and was generalized to any thickness by Vavilov [14]. The shape of the energy loss distribution for a given incident energy is shown in figure 9. The Vavilov distribution has two parameters. One is the ratio of the average energy loss ($\bar{\Delta}$) to the maximum kinematically allowed in a single collision (W_{max})

$$\kappa = \frac{\bar{\Delta}}{W_{max}} \approx \frac{\bar{\Delta}}{2m_e c^2 \beta^2 \gamma^2} \quad (34)$$

where we have used the fact that $m_\mu \gg m_e$. $\bar{\Delta}$, the average energy loss is given by (32). For 3cm of LAr and incident muons of 211MeV, $\kappa = 0.438$.

The other parameter, λ , is a universal parameter proportional to the energy loss.

$$\lambda = \Delta/\xi - (\ln(\xi/\epsilon') + 1 + C) \quad (35)$$

with Δ being the actual energy loss, $\xi = (0.19x/\beta^2)(MeV)$ for LAr), $\ln \epsilon' = 2 \ln \left[\frac{I}{(2m_e)^{1/2} \beta \gamma c} \right] + \beta^2$ and C is the Euler number ($= 0.577 \dots$). For κ values less than 0.01 the Vavilov distribution matches Landau's and for values greater than 10.0 it can be replaced by a Gaussian distribution with mean $\mu = \gamma - 1 - \beta^2 - \ln \kappa$ and variance $\sigma^2 = (2 - \beta^2)/2\kappa$ [15]. One point we note here is that in general the average energy loss is not the most probable. The event to event fluctuations in energy loss need to be taken into account when determining the average ion yield in a medium.

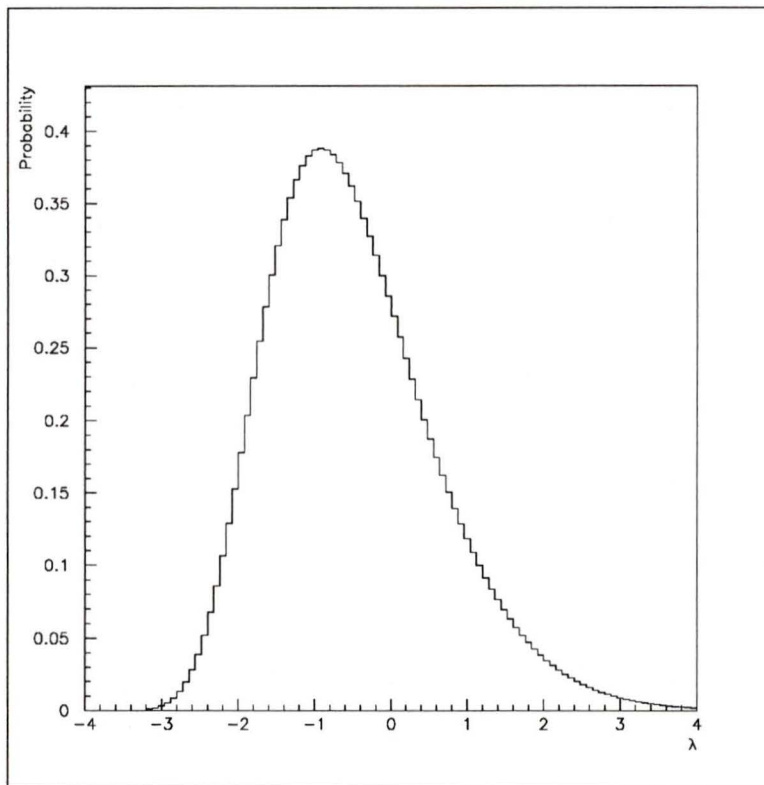


Figure 9: The Vavilov distribution for $\kappa = 0.438$ and $\beta = 0.969$. The bin size is 0.09 in λ .

3 Apparatus

3.1 Cryogenics System

The cryogenics system used in purifying and condensing the argon gas is shown in figure 10. There are two sets of three nested, axially concentric, stainless steel cylinders, one for the purification of the argon gas (sieve) and one containing the ionisation chamber (cell). The outermost cylinder is used as the vacuum insulation jacket, in which a vacuum of less than $1.0 \times 10^{-5} \text{ torr}$ was maintained by an oil diffusion pump fitted with a liquid nitrogen (LN_2) cold trap and baffle system.

The second cylinder is the LN_2 cooling jacket (see figure 11). This pot was filled with pressurized liquid nitrogen to provide the necessary cooling for the LAr cell and sieve. The cell LN_2 jacket was kept at pressures between 30 and 35 *psig*, giving a temperature of approximately 87K. For the sieve, the LN_2 was maintained at pressures above 45 *psig*, so as not to condense the argon gas as it passed through the sieve. Figure 12 shows the LN_2 temperature vs. vapor pressure curve.

The liquid level in the LN_2 jackets was controlled automatically by means of a custom built level controller (figure 13 shows a schematic of this controller). Two 50Ω composite carbon 1/8W resistors were suspended inside the LN_2 jackets, defining an upper and lower level limit. These resistors were each in series with another 50Ω resistor (1/4W). A constant voltage was applied across the resistors, giving a total power dissipation in the sensing resistors of close to 1/8W at room temperature. When the sensing resistor is in liquid nitrogen it is able to dissipate more power than in gas and hence the

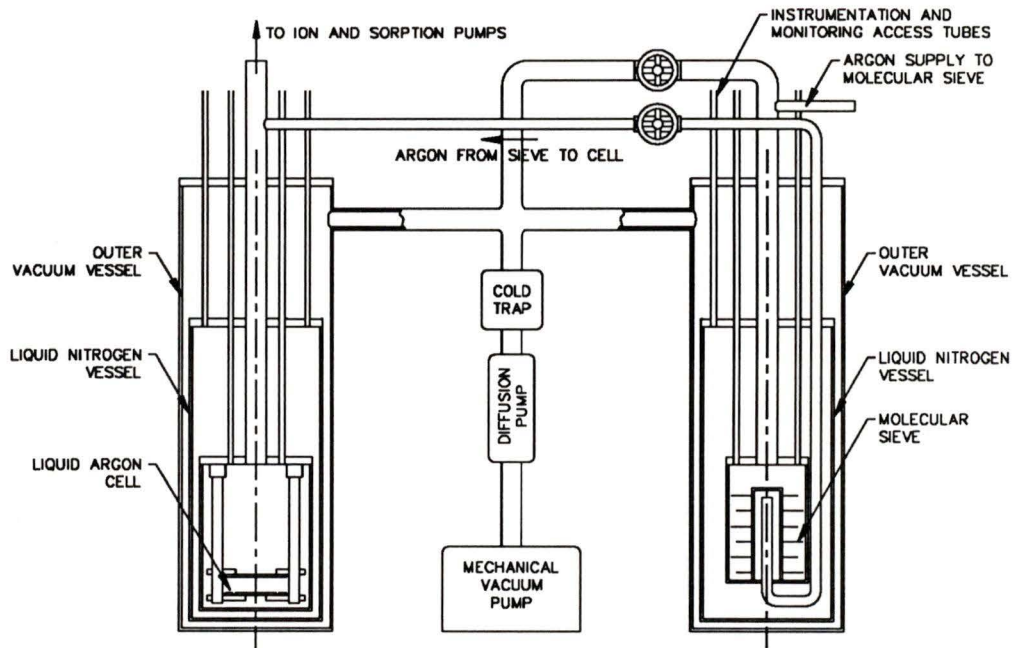


Figure 10: Schematic diagram of the LAr purification and test apparatus

voltage at the op-amp input falls closer to ground. This gas-liquid voltage difference is typically $110mV$. The operational amplifier converts the voltage levels to TTL logic levels and feeds an inverter with a Schmitt trigger input (74LS14).

The logic in the controller is such that a solenoid valve is opened allowing an N_2 gas bottle to pressurize a storage dewar and force liquid into the cooling jacket when the liquid level is below both resistors. When the level is at the upper resistor the solenoid valve is closed, stopping the transfer. In this manner a constant liquid level is maintained for cooling. Figure 14 shows the LN_2 transfer system.

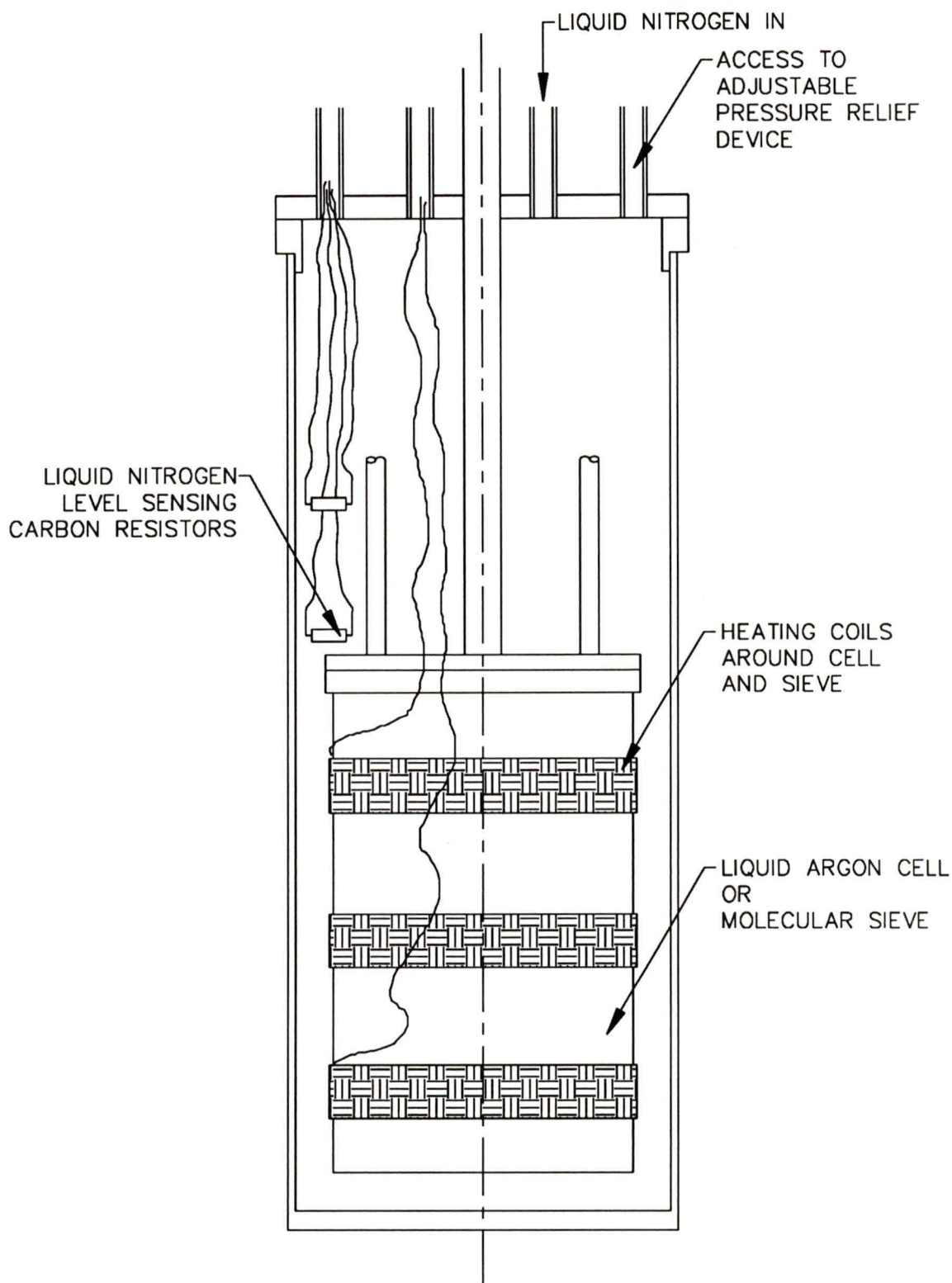


Figure 11: Schematic cross section of the LN_2 Vessel

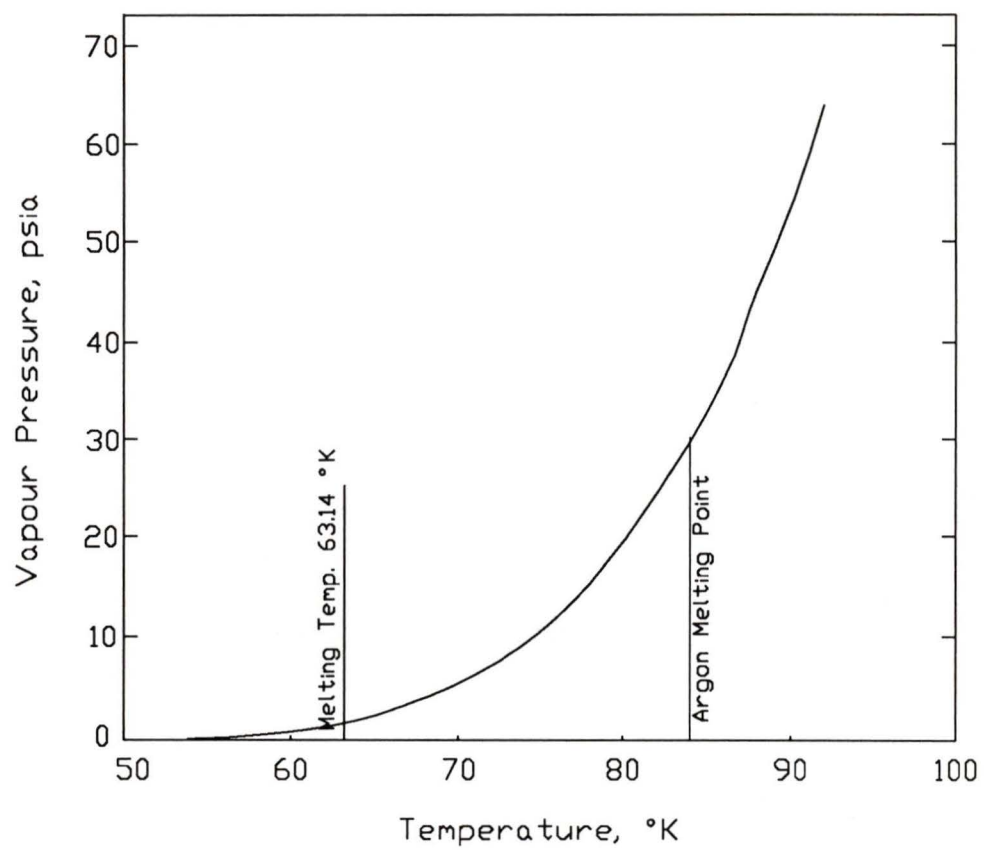


Figure 12: LN_2 Vapour pressure vs. temperature

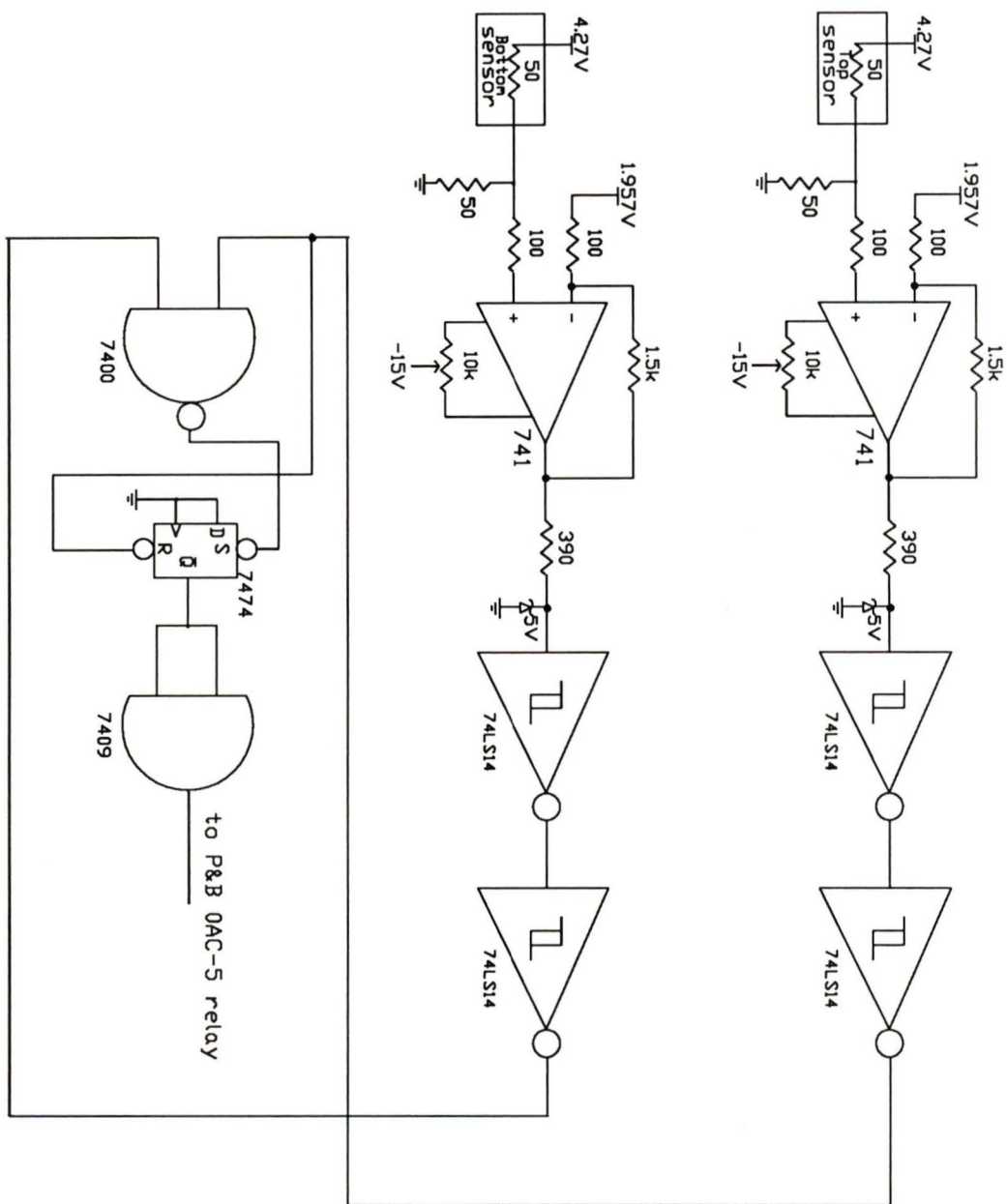


Figure 13: A schematic of the LN_2 level controller. The sensor resistors are composite carbon.

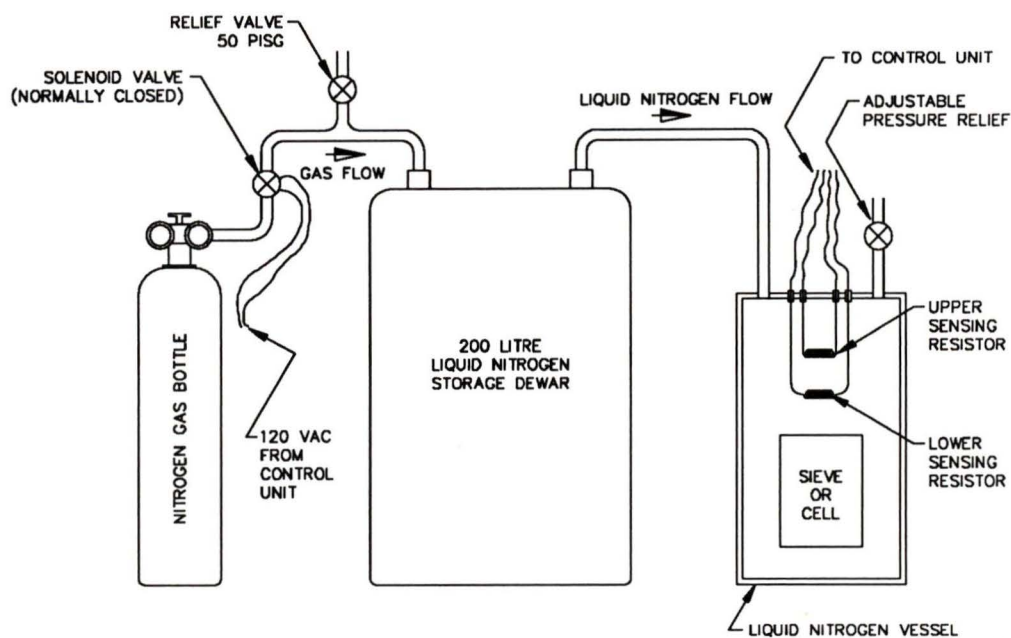


Figure 14: The liquid nitrogen transfer system

3.2 Sieve vessel and preparation

The sieve container consisted of a system of baffles forcing the argon gas to be in contact with the molecular sieve for the longest possible time, much the same as that used by Chen's group [16] (see figure 15). 4.5 pounds of molecular sieve were used consisting of an equal volume mix of 3A, 4A, 5A and 13X [19] molecular sieve. The molecular sieve consists of submicroscopic pores, inside of which there are polarized trapping sites. If a polar molecule can fit into the pore, it will be bound at these sites. The numbers 3A, 4A etc. refer to pore sizes of 3Å, 4Å etc. These sieves are used at low temperatures so as to lessen the thermal energy available for trapped materials to free themselves.

The sieve was prepared by evacuating it to 0.182 *mtorr* at 347°C, a

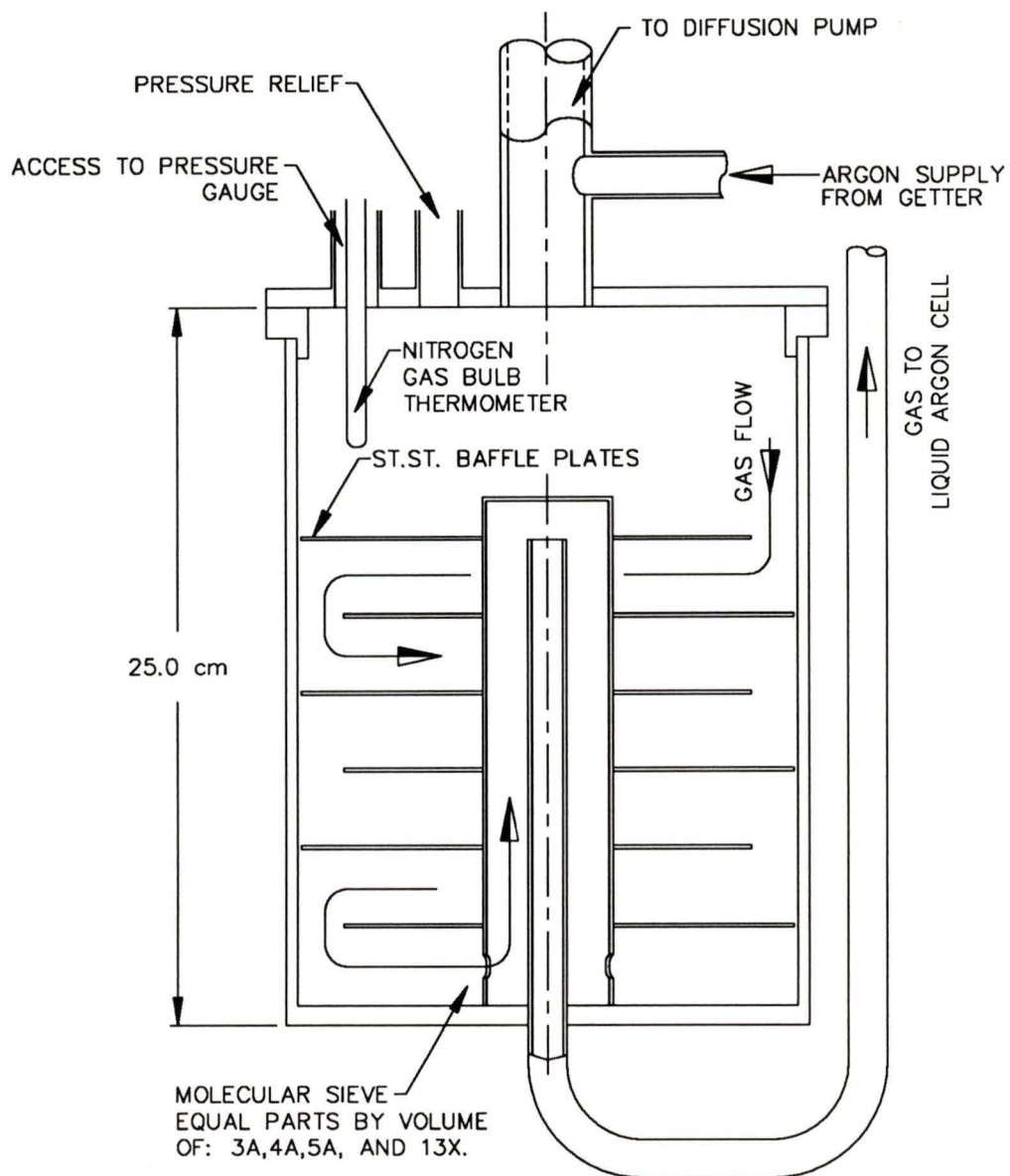


Figure 15: Schematic cross section of the sieve vessel

procedure which took 1 month. During this evacuation the temperature was kept stable to $\pm 1^\circ\text{C}$ by means of a temperature controller adapted from a thermometer described by Horowitz and Hill [17]. The temperature was controlled in this manner because of the exponential dependence of pressure on temperature in the sieve material. This effect manifested itself as day/night variations in pressure due to the day/night variations in the AC line voltage being supplied to the heating tapes.

3.3 Cell vessel and preparation

The cell chamber was a cylinder 11.5cm in radius and 33cm high, giving a total volume of 14l. All materials inside this chamber and in its various access tubes were either stainless steel, ceramic or copper. All surfaces were subjected to the same cleaning procedure. This procedure consisted of: cleaning with 95% ethanol (5% water); rinsing with 100°C distilled water; drying with warm argon gas; then rinsing with de-ionised ($> 10M\Omega/cm$) water and finally drying with warm argon gas. The various parts were then assembled and the system was evacuated with sorption pumps and an ion pump, while being baked at 250°C . The final pressure in the system was $1.02 \times 10^{-6}\text{torr}$ at 250°C which decreased to $1.47 \times 10^{-8}\text{torr}$ at 85K (the temperature of the cell when cooled). The vacuum constituents were monitored with a quadrupole mass spectrometer and the final vacuum had as its most abundant constituent, H_2 from the stainless steel walls. Water was present to less than $5 \times 10^{-9}\text{torr}$ partial pressure and O_2 was also present at pressures less than $0.5 \times 10^{-9}\text{torr}$, see figure 17. This amount of O_2 in our volume would produce approximately 2 parts O_2 in 10^9 for 10l of LAr.

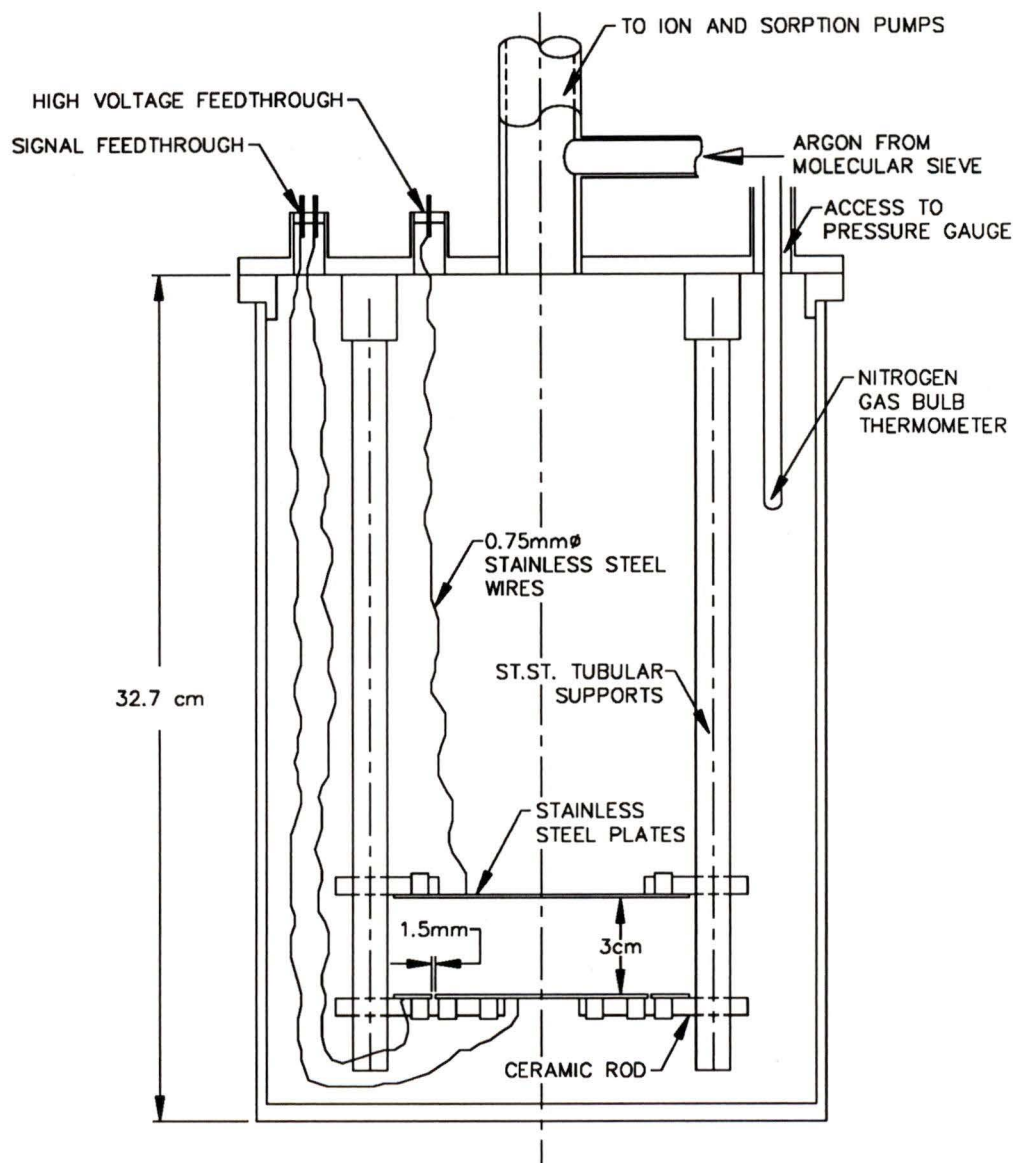


Figure 16: Schematic cross section of the LAr cell

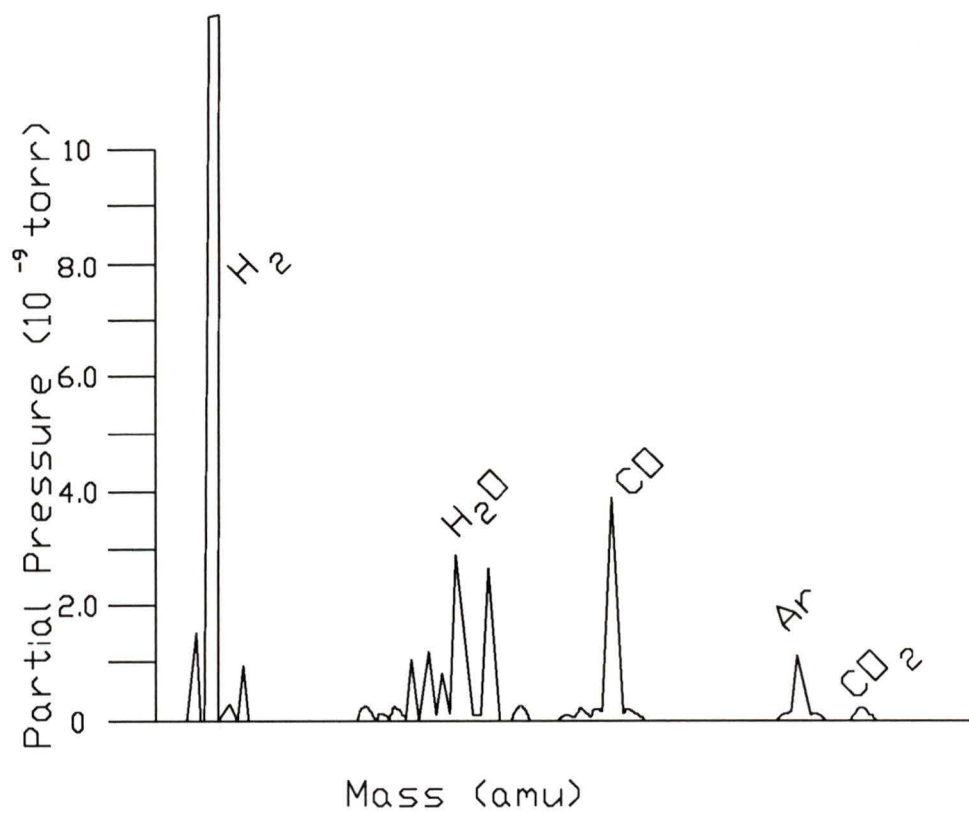


Figure 17: Residual gas in the system before filling

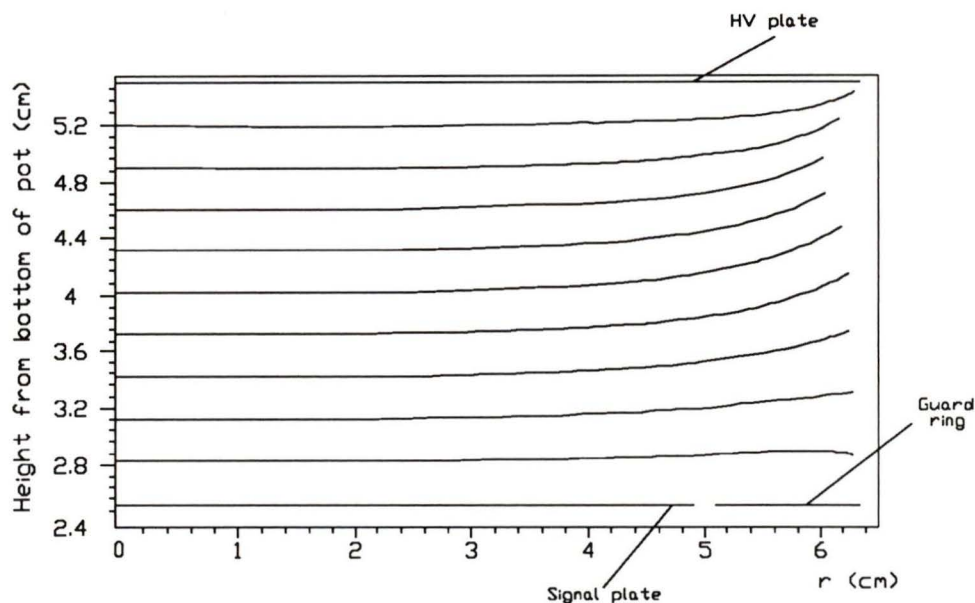


Figure 18: The lines of constant potential obtained with a 0.5mm grid.

The actual ionisation chamber consisted of two $1/16''$ (1.59mm) stainless steel plates suspended from the cell lid by means of tubes and rested on ceramic dowels (figure 16). The plates were $5''$ (12.7cm) in diameter and had 3cm of active volume between them. The top plate was held at negative high voltage and the bottom plate was grounded. The bottom ground plane was split into two sections, a guard ring and a signal plate. The guard ring had an outer diameter $5''$ (12.7cm) and inner diameter of $4''$ (10.2cm); the signal plate was $3\frac{7}{8}''$ (9.8cm) in diameter leaving a gap of $\frac{1}{16}''$ (1.5mm) in the ground plane. A relaxation type Fortran code, in cylindrical coordinates, was used to determine the resulting potentials for this configuration. As can be seen in figure 18, the lines of constant potential are parallel in the active region thus guaranteeing uniform drift distances regardless of the track position.

The sieve and cell pots were both equipped with a nitrogen gas bulb

thermometer and pressure transducer to monitor the LAr vapor pressure and the LAr temperature during purification and data taking. The temperature and vapor pressure were monitored on a PDP 11/34a and if the LAr temperature dropped below $86K$, heating tapes around the cell pot were turned on, thus warming the liquid to avoid freezing (Ar melts at $84K$). With this method of temperature control the LAr temperature in the cell varied between $85K$ and $95K$ throughout the data taking.

3.4 Argon Purification

Commercially available argon gas [20] was passed through a titanium gettering oven [21] operating at $800^{\circ}C$. This oven is designed to remove oxygen to below $10^{-6}ppm$. The gettered argon gas was passed through the molecular sieve at $5l/min$ and condensed in the cell chamber. A total of $10l$ of liquid was condensed in the cell chamber. After filling, the cell chamber was isolated from the sieve and left for two months while cosmic ray tracks were observed.

3.5 Data Acquisition System

The passage of a muon through the cell chamber was signaled by a coincidence in three $10cm \times 10cm$ plastic scintillators, one on top of the cell vacuum vessel lid and two below the bottom, thus separating the top and bottom scintillators by $115cm$. This gave us a total solid angle of approximately $7.6 \times 10^{-6}sterad$. A two $2''$ thick lead brick was placed between the bottom two counters to increase the minimum muon energy that could create a coincidence to $245MeV$ ($211MeV$ from the top of the active volume to the

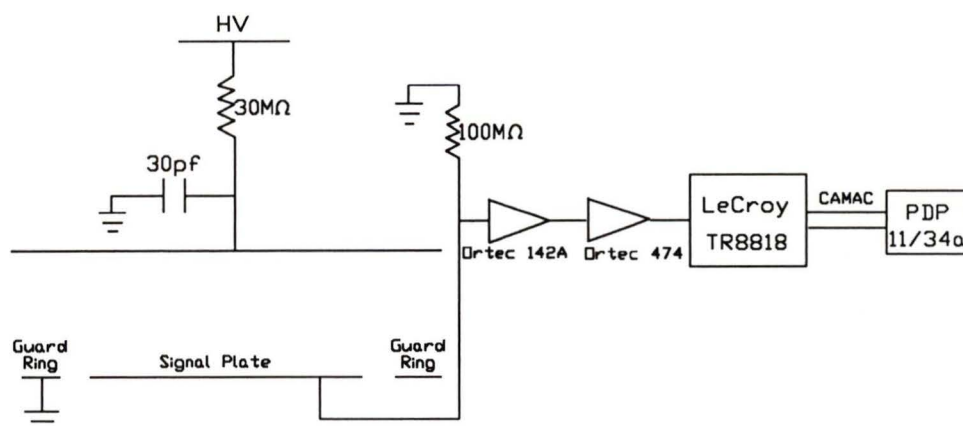


Figure 19: The data readout chain and the high voltage input.

last scintillator). This trigger system gave, on average, 15 coincidences per hour. Assuming an intensity of $0.8 \times 10^2 s^{-1} sterad^{-1} m^{-2}$, we would expect 21 coincidences per hour.

The high voltage was supplied by a Bertan 380X power supply and was filtered by an RC network as shown in figure 19. The signal readout chain is also shown in figure 19. The external bleed resistor was necessary as the Ortec 142A is an AC coupled pre-amp thus providing no ground reference for the plate. The signal from the pre-amp was then fed into an Ortec 474 timing filter amplifier with the integration and differentiation constants set equivalent to $10ns$ and $150\mu s$ respectively. The waveforms from the amplifier were digitized using a CAMAC based LeCroy TR8818 transient analyzer controlled by a PDP 11/34a computer. The sampling rate used was $80ns/sample$ and 7168 post trigger points were taken for each pulse. The TR8818 has a voltage resolution of $2mV$ with a dynamic range of $511mV$.

The transfer function of the acquisition system was measured by applying a step input (risetime $\approx 10ns$) at the test input of the pre-amp. Since

this input has a $1pF$ capacitor between it and the signal input, this is identical to applying a delta current pulse on the input. This signal was processed through the entire readout chain and then analyzed. A total of 64 samples were taken for the transfer function and averaged together. The resulting average was scaled to 10^4 electrons input.

Data was taken at two different gain settings and the transfer function was measured for each. The transfer function was digitized at $10ns$ sampling period for 7168 post trigger samples, and then a fit to expression (50) of appendix A was made for each. The two functions and their fits are shown in figures 20 and 21. For the $\times 4$ gain setting we found the parameters in (50) to be

$$\begin{aligned}
 \tau_1 &= (41 \pm 6)\mu s \\
 \tau_2 &= (28 \pm 2) \times 10^{-3}\mu s \\
 \tau_3 &= (0.12 \pm 0.01) \times 10^3\mu s \\
 A &= -0.10 \pm 0.03 \\
 B &= -0.30 \pm 0.11 \\
 C &= -2.24 \pm 0.02
 \end{aligned}
 \tag{36}$$

normalized to 10^4 electrons input. For the $\times 6$ setting

$$\begin{aligned}
 \tau_1 &= (1.024 \pm 0.001) \times 10^{-3}\mu s \\
 \tau_2 &= (31 \pm 6) \times 10^{-3}\mu s \\
 \tau_3 &= (0.12 \pm 0.03) \times 10^3\mu s \\
 A &= (-0.12 \pm 0.02) \\
 B &= (-0.8 \pm 0.1) \\
 C &= (-2.21 \pm 0.03)
 \end{aligned}
 \tag{37}$$

yielded the best fit to the data, again normalized to 10^4 electrons input. We note that since the Ortec 474 timing filter amplifier was set to an integrating time of $10nS$ and a differentiating time of $150\mu S$, our values for τ_2 and τ_3

Voltage (V/cm)	Gain	$T_{start}(K)$	$T_{end}(K)$	Noise (e's)	# of triggers
-1000	$\times 4$	86.5	90.0	5400	200
-400	$\times 4$	88.7	89.3	12000	209
-333	$\times 4$	86.5	86.5	9900	86
-200	$\times 6$	86.8	88.4	10000	241
-100	$\times 4$	86.2	88.4	5400	253
-40	$\times 6$	86.6	89.5	11000	342
-30	$\times 4$	88.1	86.5	10000	231

Table 1: The number of pulses taken at each voltage and the conditions

above are quite consistent with these settings.

The noise at the output was measured for each voltage using a pulser at the test input with a $5\mu s$ risetime. For these measurements the amplifier was read out by a LeCroy 3001 qVt. The noise was seen to be fairly independent of voltage, ranging from 5400 to 12,000 electrons *rms* (see table1). This is an acceptable noise level as the charge expected from a minimum ionising muon is 258,000 electrons. The major noise source was identified as due to acoustic noise from the LN_2 pressure release valve.

3.6 Data Taking

Data was taken at voltages ranging from $1kV/cm$ to $30V/cm$ (see table 1). Each voltage run lasted on average 17 hours. Before each run the temperature was recorded and the LN_2 jacket was filled. The data acquisition was left running overnight and stopped in the morning. Then the temperature of the LAr was again recorded and the number of events logged. After the data acquisition was finished the noise at the voltage was measured and recorded.

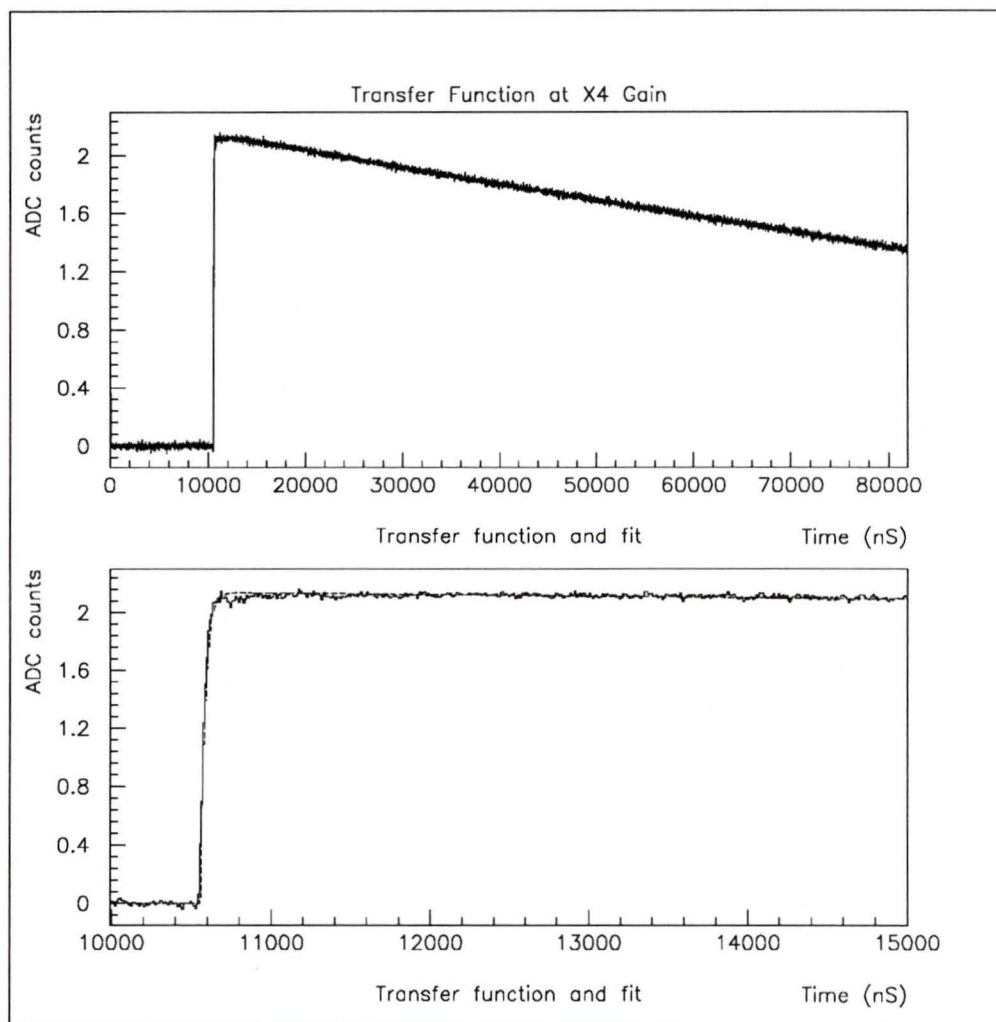


Figure 20: The transfer function at $\times 4$ gain normalized to 10^4 electrons input, with the fit superimposed. The bottom picture is an expansion of the top.

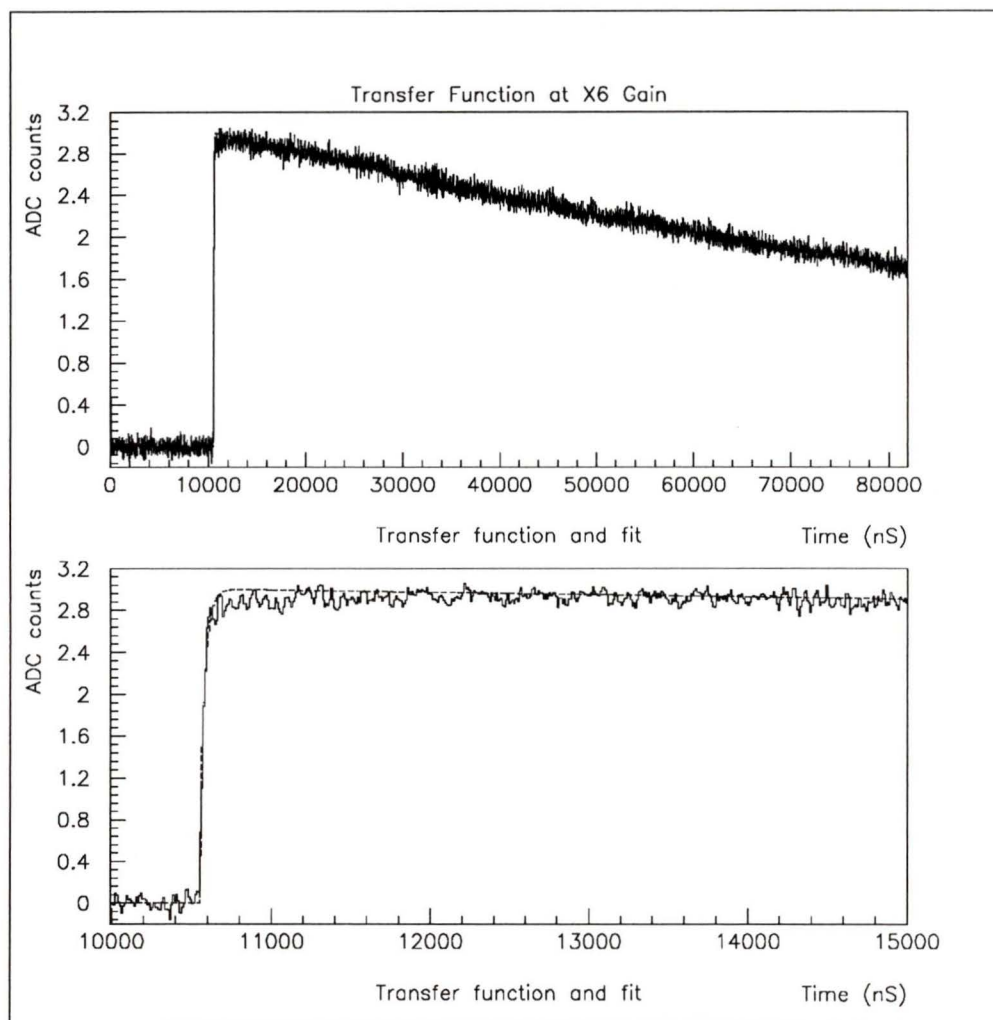


Figure 21: The transfer function at $\times 6$ gain normalized to 10^4 electrons input, with the fit superimposed. The bottom picture is an expansion of the top.

4 Data Analysis

4.1 Initial Data Selection

A typical pulse from our *LAr* cell is shown in figure 22. The rise starts at approximately $82000ns$ (1025 digitizations from zero or $80ns$ after the trigger) and ends approximately $21\mu s$ later, followed by the exponential decay expected from equation (53) in Appendix-A. The pre-trigger portion of the pulse is centred at 42 ADC counts because the ADC zero was set at a negative voltage. From table 36 we see the rms noise at this voltage was measured to be 10^4 electrons or, using the pulse height in figure 21, 3 ADC counts, quite consistent with the noise seen on the pulse.

From our raw data sample many pulses needed to be rejected. Some triggers could occur with no particle passing through the chamber, due a mismatch in the geometry of the trigger scintillators (square) and the detector (cylindrical). For the same reason, some pulses were seen to be inverted. These inverted pulses were caused by tracks in the guard ring region, the signal resulting on the guard ring was capacitively transferred to the signal line, thus producing an opposite pulse. Taking the area covered by the scintillators as compared to the active cell region, we would expect approximately 30% of all triggers to be misses due to this geometry mismatch.

As well as rejecting these missed pulses it was found that many of the pulses showed a saturation effect. This caused the peaks of the pulses to remain flat over several microseconds. This saturation was independent of pulse height and can be attributed to noise saturating the pre-amp at frequencies well below the $3dB$ point of the amplifier.

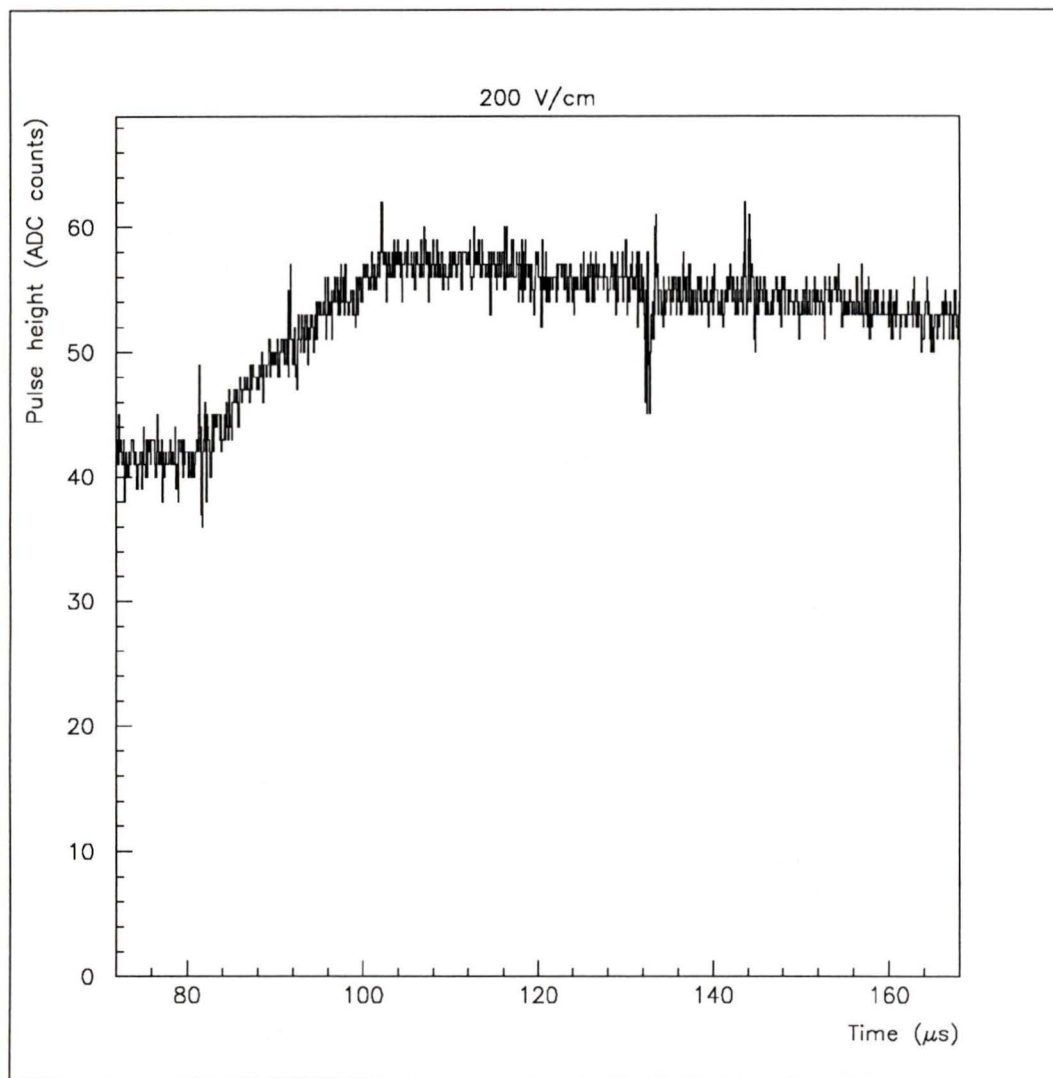


Figure 22: A typical pulse as digitized by the transient analyzer

To reject the unwanted pulses before analysis, each recorded event was analyzed prior to pulse shape fitting. For each pulse the analysis chain was as follows. The pulse was baseline shifted to zero by calculating the average ADC channel of the first 1000 pre-trigger points. Next the integral of the pulse rise from the 1024th to the 1824th bin was calculated by summing these counts. Also as a measure of pulse height, the data pulse was convoluted with a theoretical response function of an integrator and differentiator of equal time constants of 1000 μ s. This should give a good signal to noise ratio [18]. The peak height of this resulting waveform was then found. Next, to reject the saturated pulses, a region starting from 4 μ s before the expected peak position to 360 μ s after, was fit to a flat line and the χ^2 of this fit was calculated.

To be selected for further processing, each event had to pass three cuts. The first two were coupled together, being cuts on the integral of the pulse rise and on the convoluted pulse height. A sample scatter plot of these two variables is shown in figure 23. The cuts were chosen so as to separate the clear pedestal portion from the good data. The clear band evident in this plot indicates that both these measurements are indeed correlated.

The final cut was made to reject the saturated pulses, which we expect to favour no particular pulse height. To do this the χ^2 plot was cut at the low end where there was a clear indication a flat peak (see figure 24). Figure 25 which shows the convoluted pulse height spectrum with the two pulse height cuts and then with these two cuts and the flatness cut, demonstrates that this cut did not introduce any bias on the measured pulse height.

Table (2) shows the number of pulses for each voltage that pass these cuts.

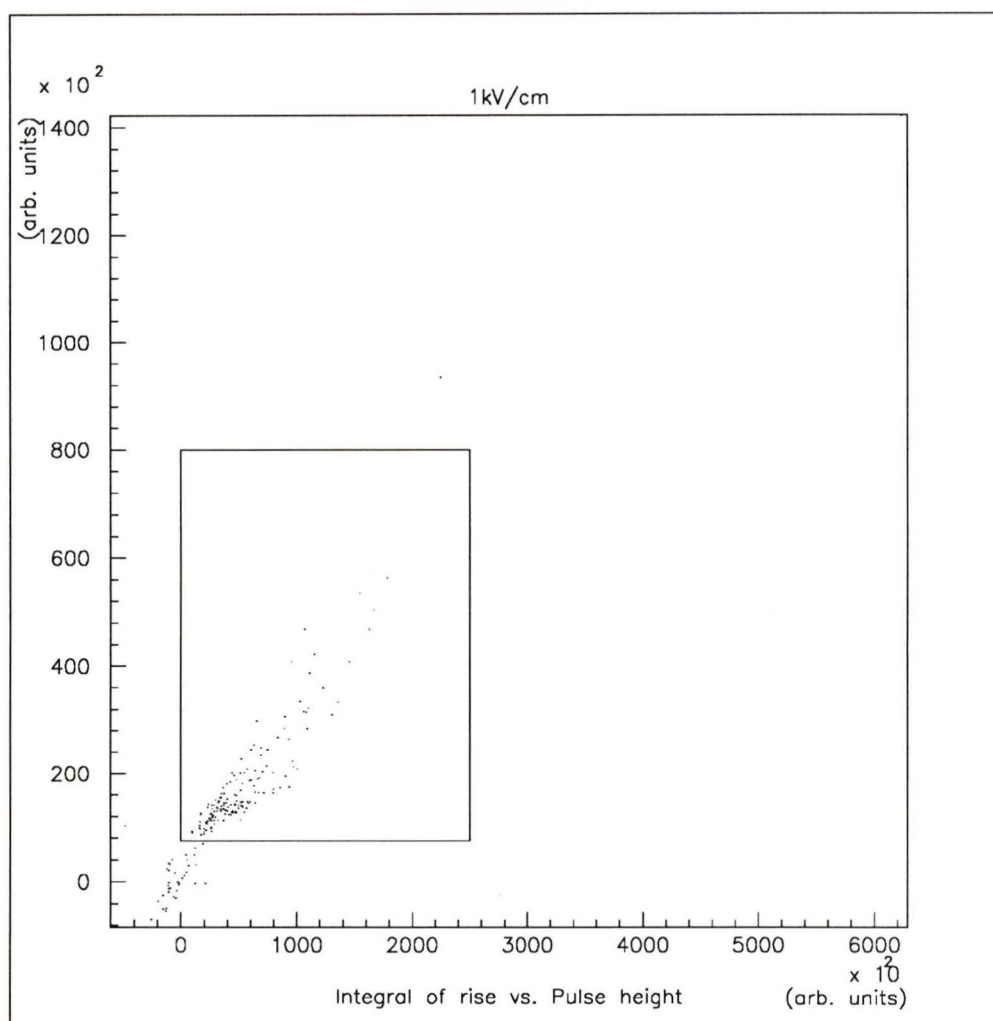


Figure 23: The integral of the pulse rise vs. the pulse height. The points inside the box make the cuts on these two variables.

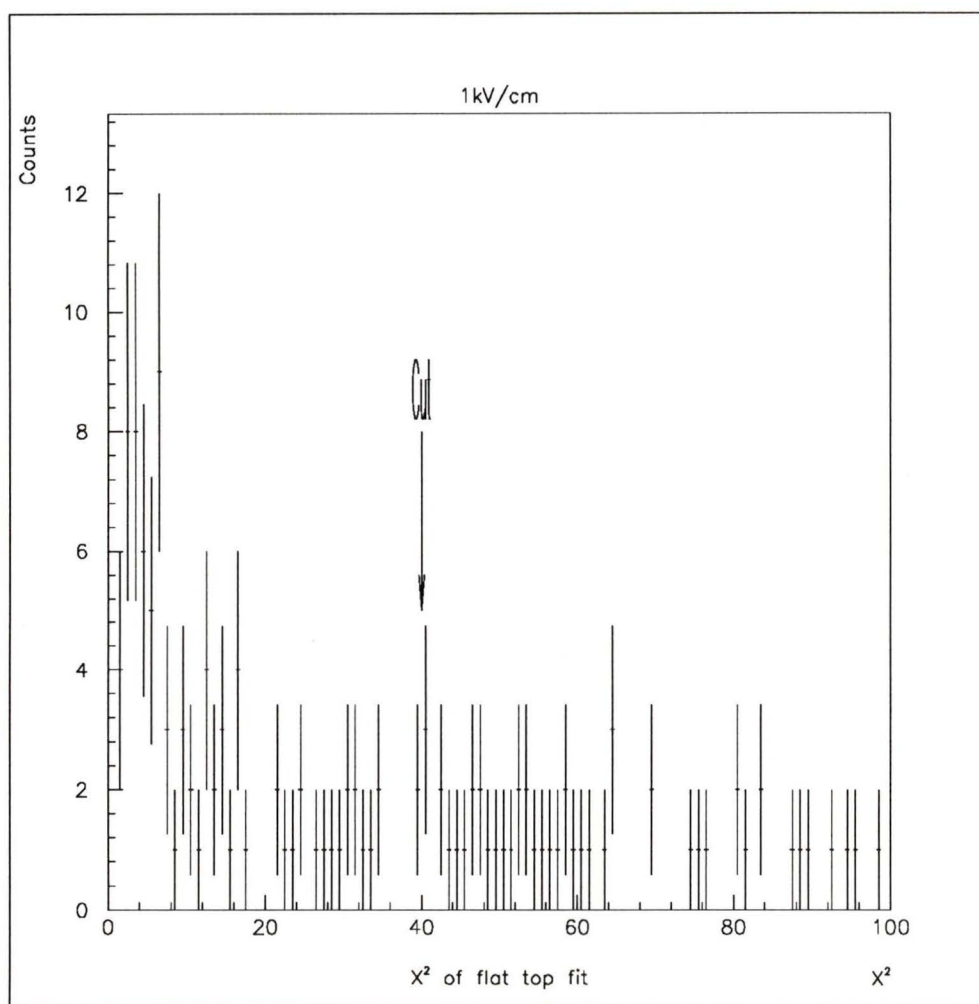


Figure 24: The χ^2 of the fit to a flat peak. The arrow shows where the cut was made.

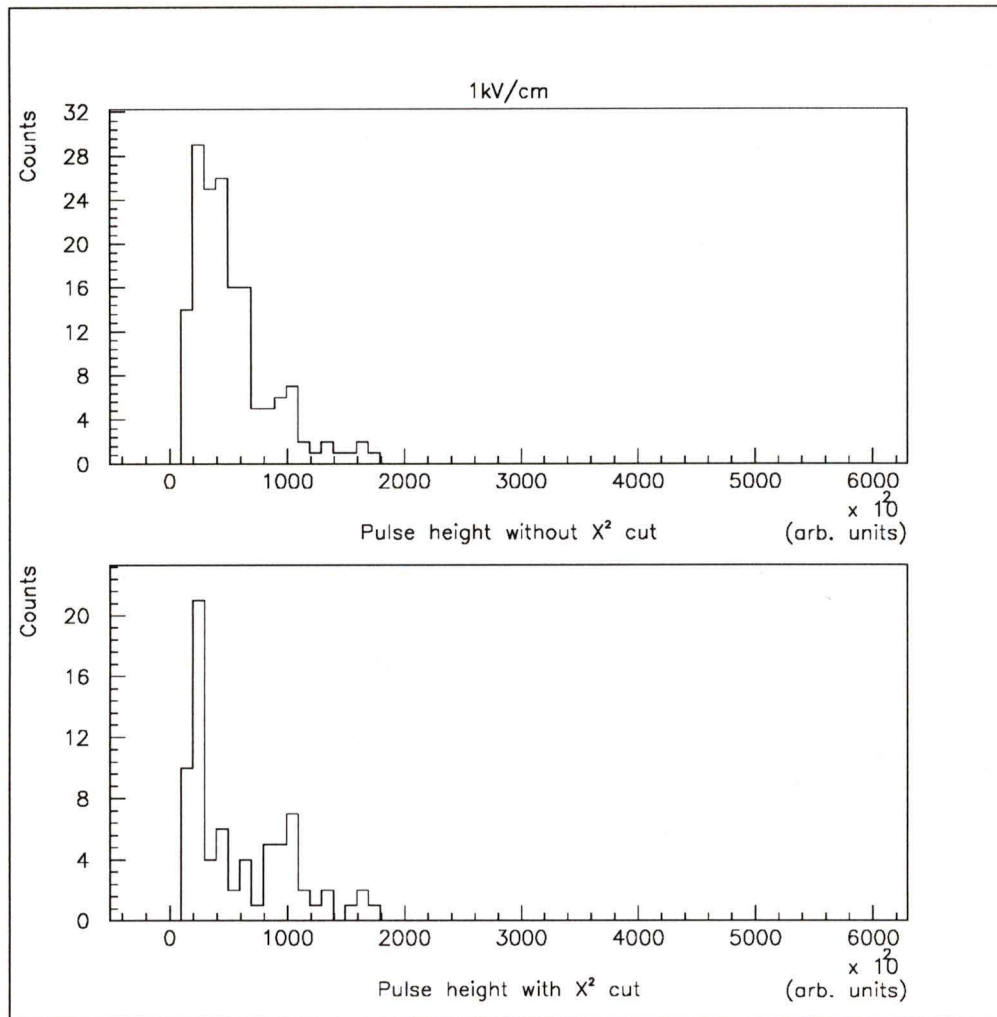


Figure 25: TOP: The pulse height spectrum with the two pulse height cuts. BOTTOM: The same with the χ^2 cut.

Voltage (V/cm)	# in raw sample	# that pass cuts	% pass cuts
-1000	200	74	37
-400	209	26	12
-333	86	24	28
-200	241	93	39
-100	253	42	17
-40	342	108	32
-30	231	56	24

Table 2: The number of pulses at each voltage that pass the cuts

4.2 Determination of the drift velocity and the electron lifetime

After the initial data selection the pulses that passed the cuts were averaged together. Because of the fluctuations in the number of electron-ion pairs produced in each event, a direct average could not be used. Instead we multiplied each pulse by $10^4/PH$, with PH being the pulse height found using the convolution. A sample resulting average is shown in figure 26.

Before fitting the pulse it was necessary to re-evaluate the noise for this average, as the scale factor was not known precisely. To do this the variance of the first 1000 digitizations from zero was used as the square of the rms noise. Then the average pulse was fit using the MINUIT function minimization routine [22] to equation (51), which is

$$V_0(t) = \begin{cases} 0 & t < 0 \\ [A + B]c(\tau_1) + [C - A]c(\tau_2) - [B + C]c(\tau_3) & 0 \leq t \leq \tau_d \\ [A + B]\gamma(\tau_1) + [C - A]\gamma(\tau_2) - [B + C]\gamma(\tau_3) & t > \tau_d \end{cases} \quad (38)$$

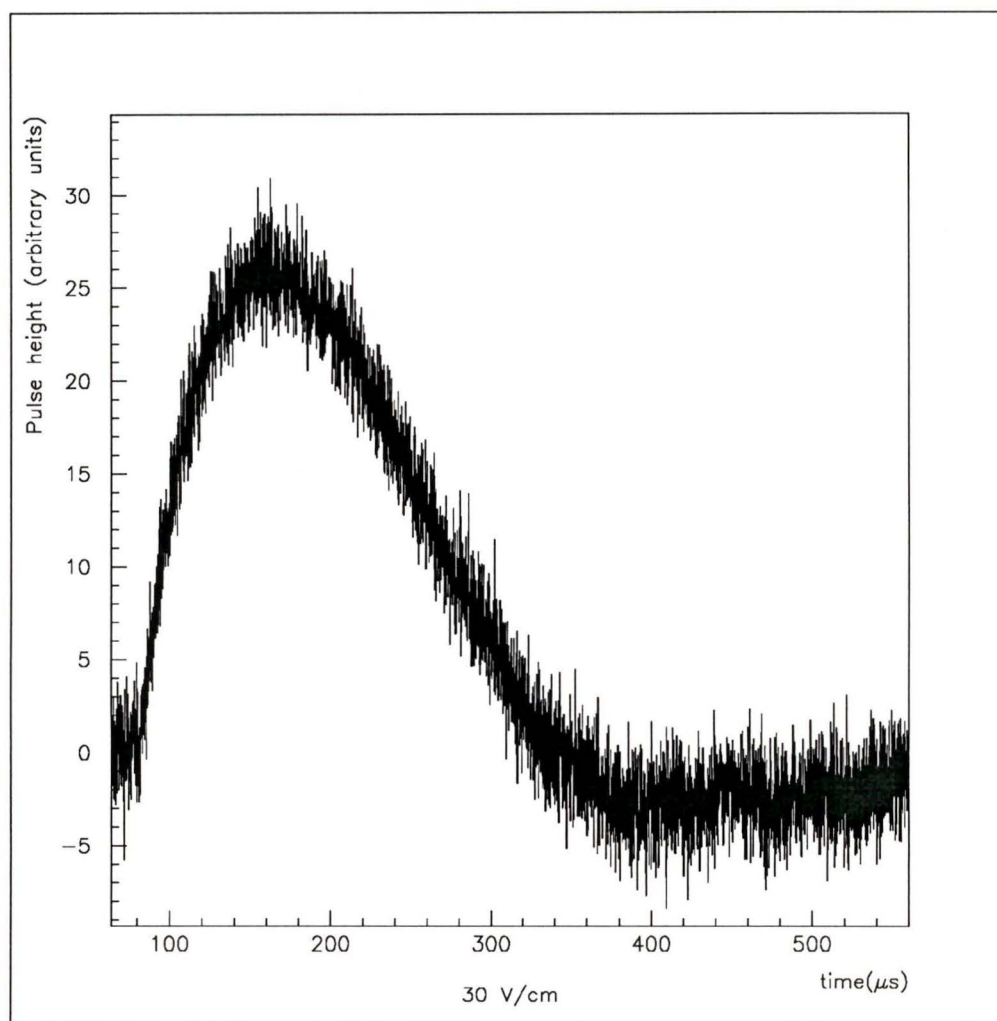


Figure 26: A sample average obtained. Notice that the tail falls below zero.

where

$$c(\tau_1) = \frac{1}{a} \left\{ e^{-t/\tau} - e^{-t/\tau_1} - \frac{1}{a\tau_d} \left[e^{-t/\tau}(at - 1) + e^{-t/\tau_1} \right] \right\} \quad (39)$$

$$a \equiv \left(\frac{1}{\tau_1} - \frac{1}{\tau} \right)$$

and

$$\gamma(\tau_1) = \frac{e^{-t/\tau_1}}{a} \left[\frac{1}{a\tau_d} (e^{a\tau_d} - 1) - 1 \right] \quad (40)$$

The various constants A,B,C, τ_1 , τ_2 and τ_3 are those from the fit to the transfer function. The fits had four parameters; the electron drift time, the electron life time, the (amplified) number of free electrons, and t_0 , the starting time for the pulse rise. Each average was fit from the 800th digitization until a point after the pulse rise.

The exact choice of where to end the fit was found to influence the resulting answer. In theory equation (38) should give the pulse shape for all times. This is true, however, if the transfer function is known exactly or at least, quite well. We found that, although the fits to our transfer functions were quite good (see figures 20 and 21), at times after the pulse rise the pulse would fall off faster than our fit to the transfer function would allow. This can be attributed to our assumption of equation (50) for our transfer function. This equation corresponds to perfect RC integrators and differentiators, whereas a real amplifier is far from ideal. The major manifestation of this assumption is that (50) cannot produce a fall that goes negative and then back to a baseline, as our pulses do (see figure 26).

We can only fit our pulses confidently for 70 μs after t_0 as we have a valid transfer function for only 71.68 μs . This won't affect our fits to pulses with risetimes much less than this (1kV/cm, 400V/cm, 333V/cm, 200V/cm),

E(V/cm)	Number of points in fit	drift time (μs)	life time (μs)
-1000	601	17.18 ± 0.06	67.23 ± 5.92
-400	601	24.78 ± 0.42	29.79 ± 2.96
-333	501	15.61 ± 0.34	$(1.0 \pm 0.5) \times 10^6$
-200	901	32.61 ± 0.18	109.22 ± 12.65
-100	1001	55.24 ± 0.17	91.96 ± 0.9
-40	2301	114.96 ± 1.15	116.87 ± 3.63
-30	2001	153.44 ± 5.37	95.15 ± 6.33

Table 3: The fits for the drift time and lifetime for the voltages. The errors are the statistical errors in the fit.

but will indeed affect our fits for the lower voltages, since at the low fields the pulse rise is more than $70\mu s$ long. With this in mind, for each pulse many different times were tried. The one chosen was the one that produced a fit with the minimum reduced χ^2 and was no longer than $70\mu s$ after the pulse peak. Figure 27 shows the variation of the reduced χ^2 versus the number of points in the fit for $30V/cm$. Notice that for fits that exceed $70\mu s$ after the peak the reduced χ^2 grows rapidly, reflecting the fact that we are fitting the fall with the incorrect function. Figures 28 to 34 show the various averages and their fits, and table 3 shows the various fit values.

From these fits the drift velocity was calculated and is plotted in figure 35. We have taken as the dominant experimental uncertainty, the variation of the mobility with temperature (20% in our temperature range). Taking a straight line fit through our four points below $300V/cm$ we find the low field electron mobility to be

$$\mu_e = (451 \pm 1 \pm 68)cm^2/Vs \quad (41)$$

for our LAr sample, which is consistent with a temperature of $91K$ (see figure

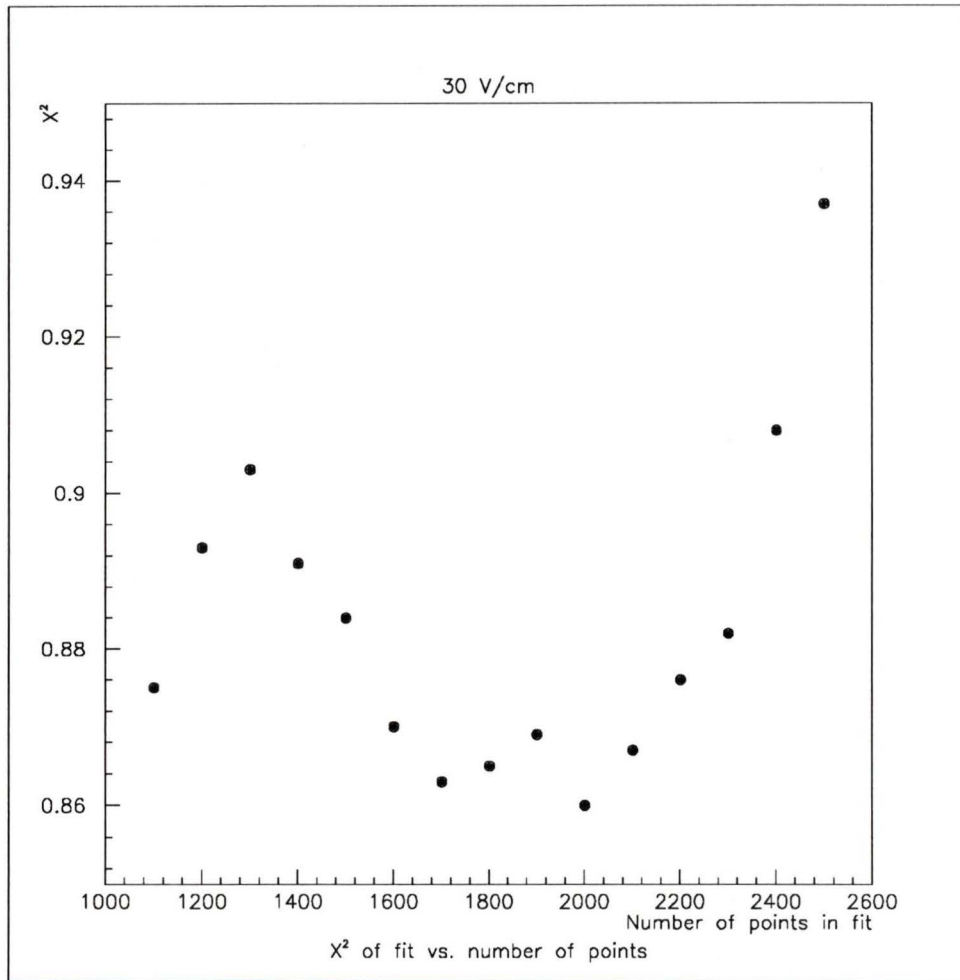


Figure 27: The χ^2 of the pulse fit vs. the number of points in the fit. The pulse peaks at 1300 and the transfer function cutoff is at 2100.

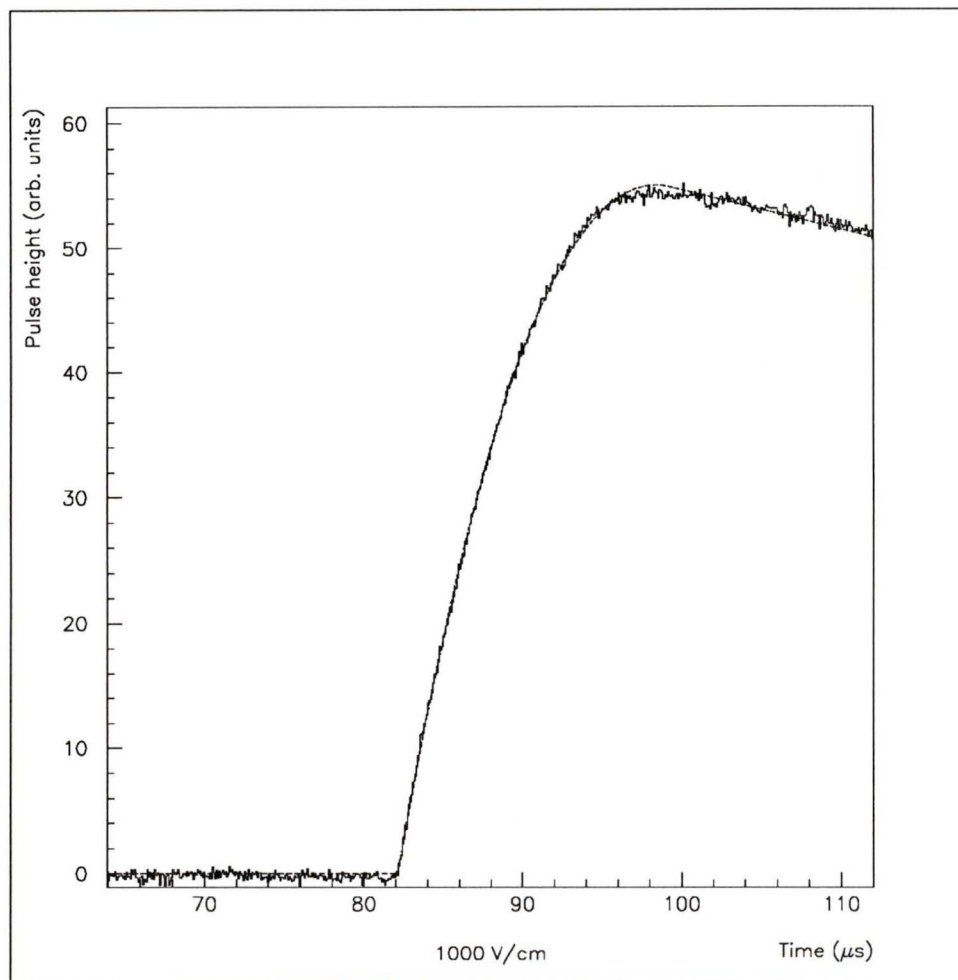


Figure 28: The averaged pulse at 1000 V/cm with the fit superimposed.

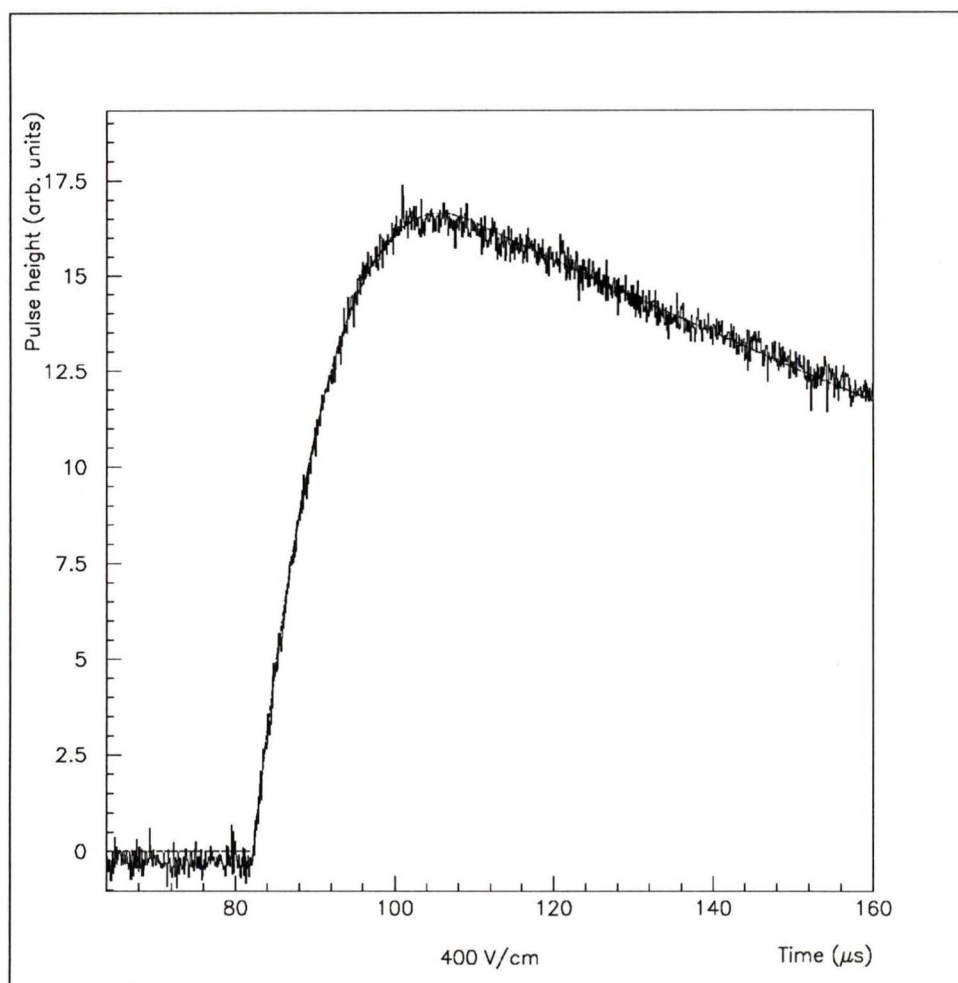


Figure 29: The averaged pulse at 400 V/cm with the fit superimposed.

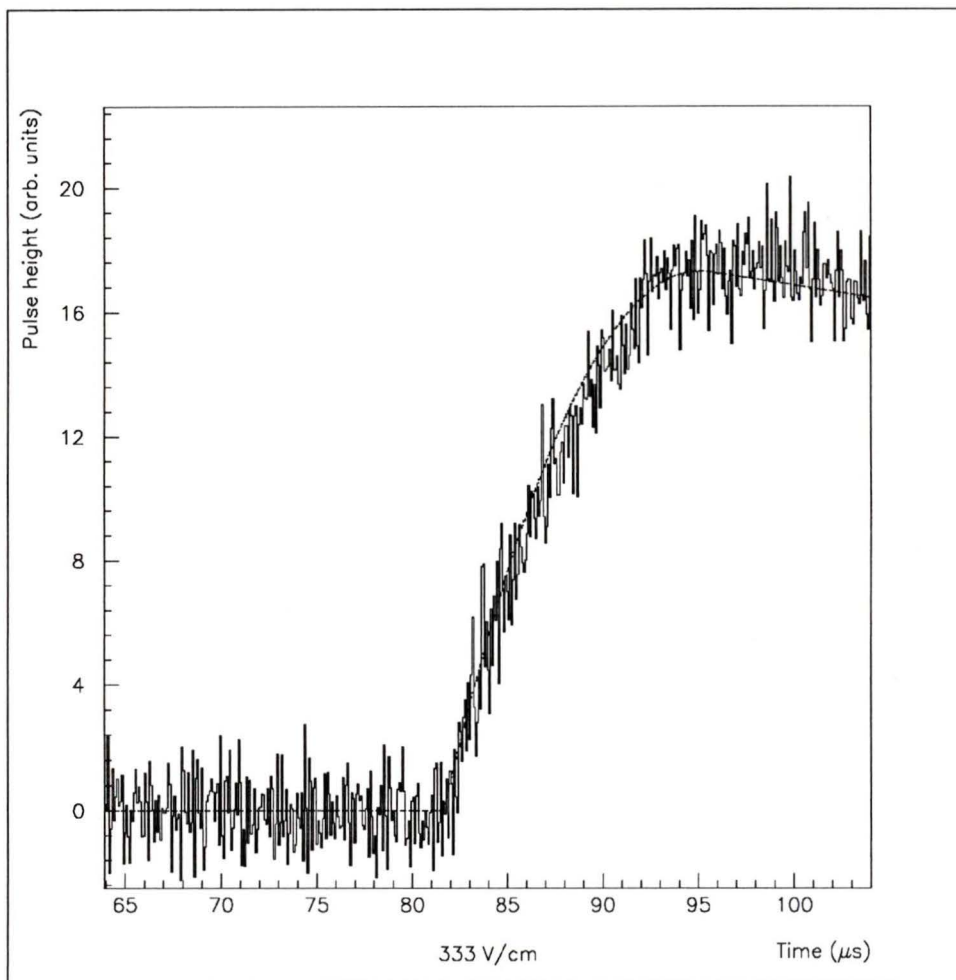


Figure 30: The averaged pulse at 333 V/cm with the fit superimposed.

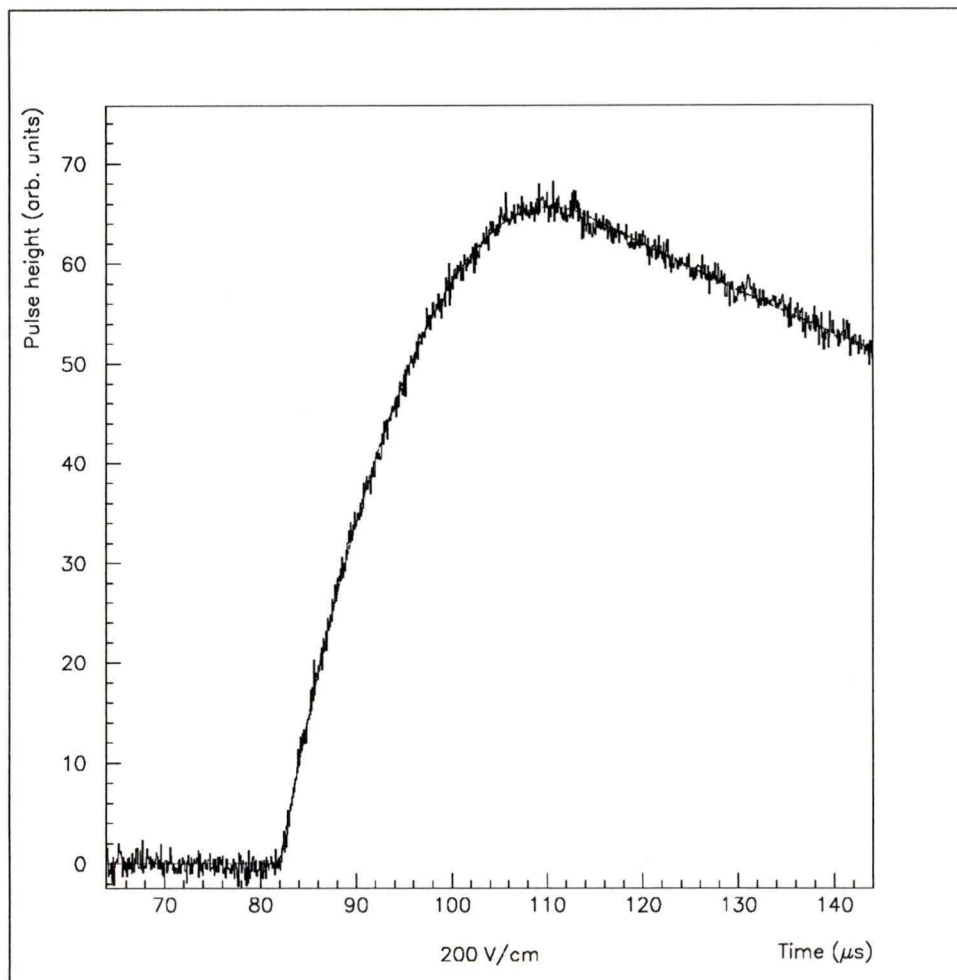


Figure 31: The averaged pulse at 200 V/cm with the fit superimposed.

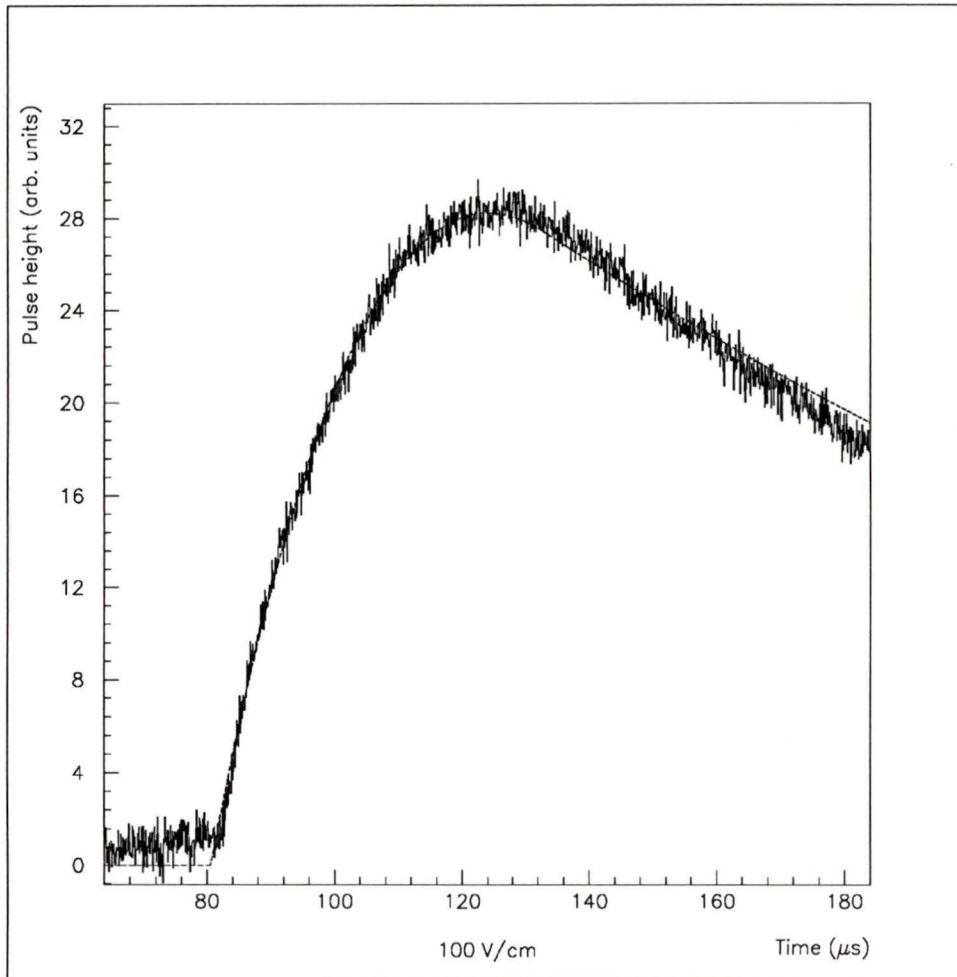


Figure 32: The averaged pulse at 100 V/cm with the fit superimposed.

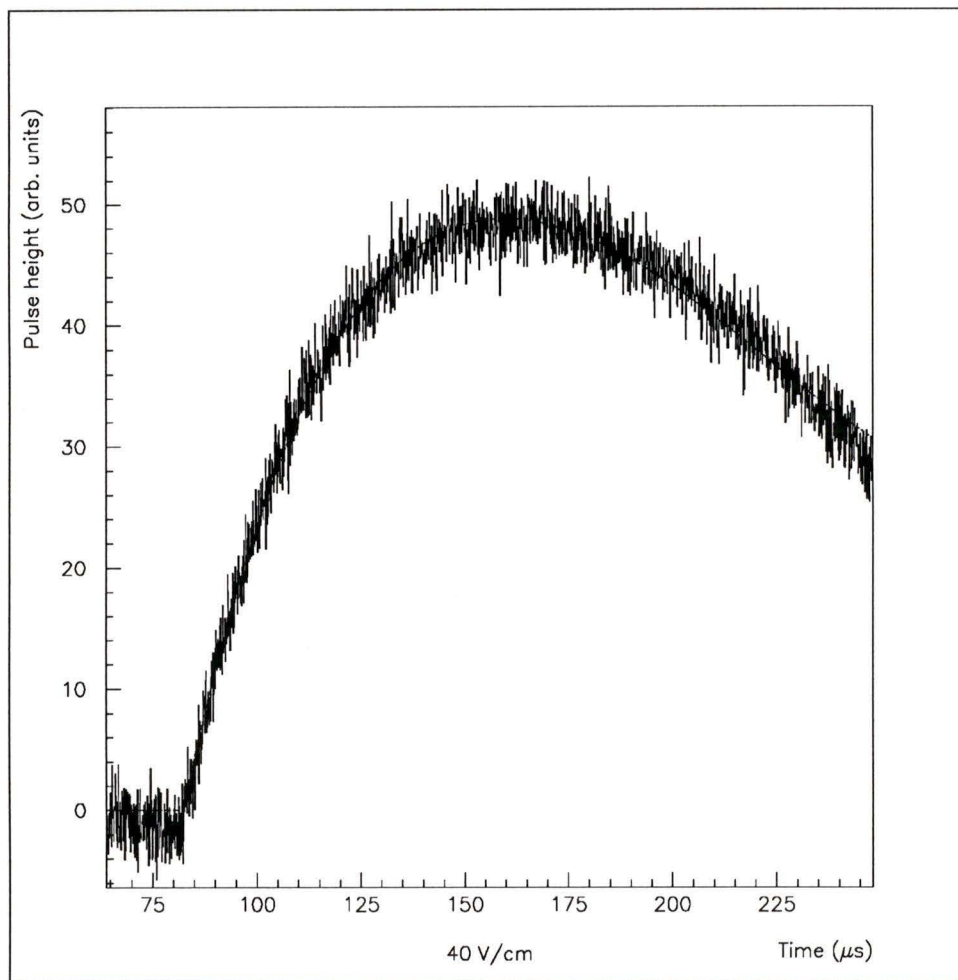


Figure 33: The averaged pulse at 40 V/cm with the fit superimposed.

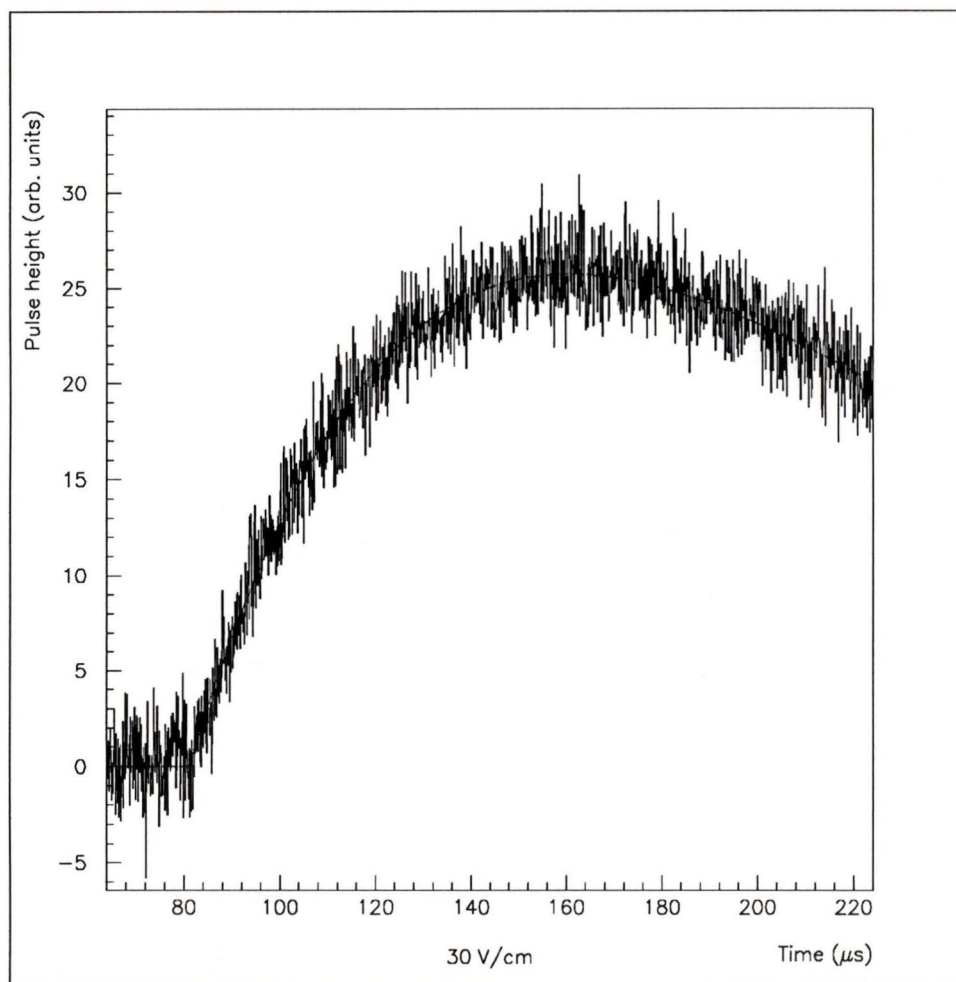


Figure 34: The averaged pulse at 30 V/cm with the fit superimposed.

7). The first error is the statistical error in the fit and the second error is the systematic uncertainty arising from an inaccurate knowledge of our transfer function. We find that our answer for the drift time can vary up to 15%, depending on the number of points in the fit. The fall off of the drift velocity at the higher voltages is in agreement with the data in figure 6.

To determine the lifetime we take the value obtained at $30V/cm$, since the longer the drift time the more sensitive to the lifetime we become. This is because we have to distinguish between the pulse peaking as $(t/\tau_d - t^2/\tau_d^2)$ or as $e^{-t/\tau}$. So we find that for our LAr sample the electron lifetime is

$$\tau = (95.2 \begin{matrix} +7.1 \\ -6.9 \end{matrix} \pm 43)\mu s \quad (42)$$

The last uncertainty is our systematic error, it reflects the fact that if we vary the number of the points in the fit out to 2300, the measured lifetime increases to $138.4\mu s$ and if we take 1700 points we get $74.8\mu s$. The first errors are the statistical errors in the fit. The measured lifetime translates into an attenuation length of 1.9 cm at $30V/cm$, or using (28), an impurity concentration of 2.36 ppb O_2 equivalent, quite consistent with the 2 ppb we estimated from the residual gas in our cell vessel.

4.3 Determination of the Absolute Charge Yield

To determine the actual charge yield as a function of the applied electric field, we fit each pulse that passed the cuts in the previous section using the known drift time and lifetime, to determine N, the number of free electrons. Since the energy absorbed by the LAr in the cell is distributed according to the Vavilov distribution, we would expect N to be as well. That this is the

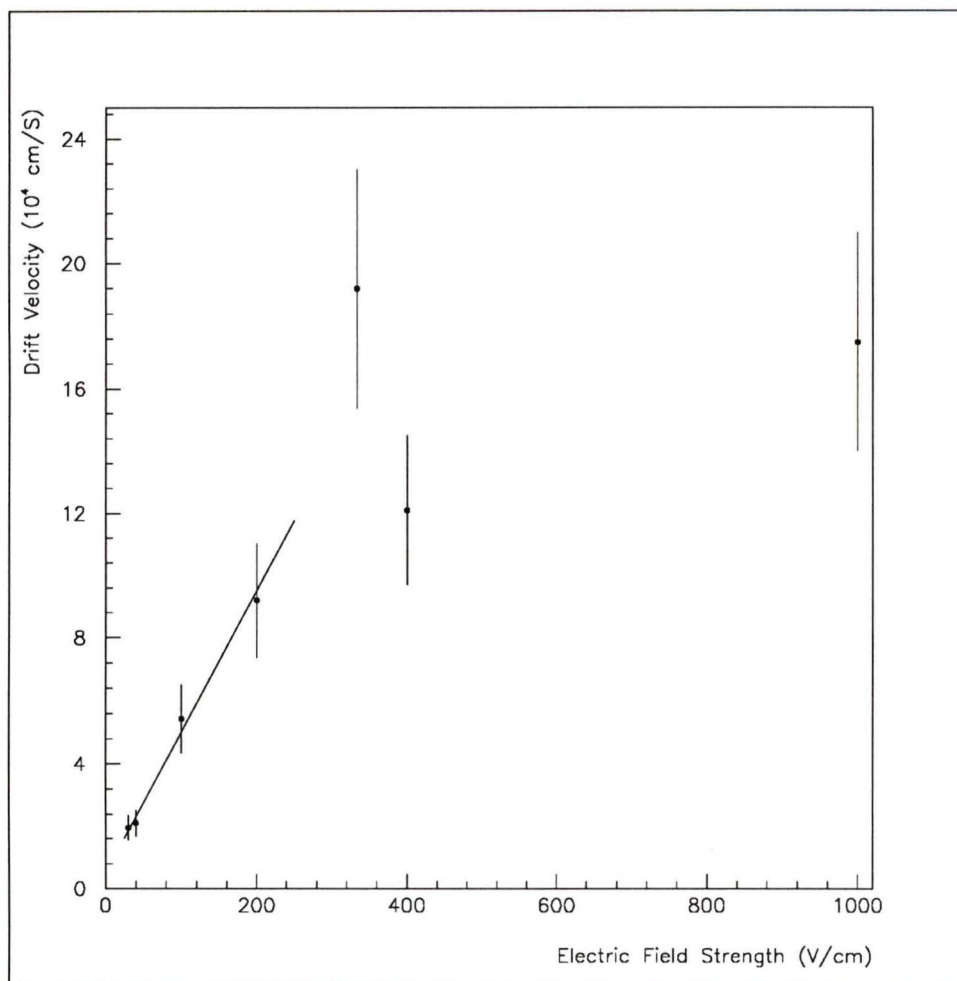


Figure 35: The Drift velocity vs. Electric field for out LAr sample. The line corresponds to $\mu_e = 451 \text{ cm}^2/\text{Vs}$.

case can be seen in figure 36.

The number of free electrons in the cell is given by

$$N(E) = \Delta \bullet G_{fi}(E) \quad (43)$$

with Δ being the energy deposited and $G_{fi}(E)$ is the field dependent conversion factor, giving the number of free electrons created per $100eV$ of absorbed energy.

For a muon to cross through the active volume and be counted it must have, on average, $211MeV$ as it enters the LAr gap. We produced 1000 random events with probability varying as $1/(energy)^2$, from $211MeV$ to $10GeV$ and for each event we generated a random energy deposition, by assuming a Vavilov distribution of the proper κ . The resulting energy deposition spectrum is shown in figure 37. To determine $G_{fi}(E)$ we sought the scale conversion that would best fit our $N(E)$ distributions. This scale conversion was found by convoluting the energy deposition spectrum with a Gaussian of standard deviation given by the rms noise at the voltage. Then a log-likelihood function was maximized assuming Poisson statistics for each bin in the $N(E)$ distribution. The resulting variation of G_{fi} with field is shown in figure 38. In figure 38 we have plotted the data of Doe's group [23] by normalizing their charge collected to our G_{fi} at $1kV/cm$. We are confident in our absolute normalization for G_{fi} since for LAr the electron yield is 3.16 electrons per $100eV$ at $1kV/cm$ [24] and we obtain $3.2^{+0.2}_{-0.6}$ for the same field.

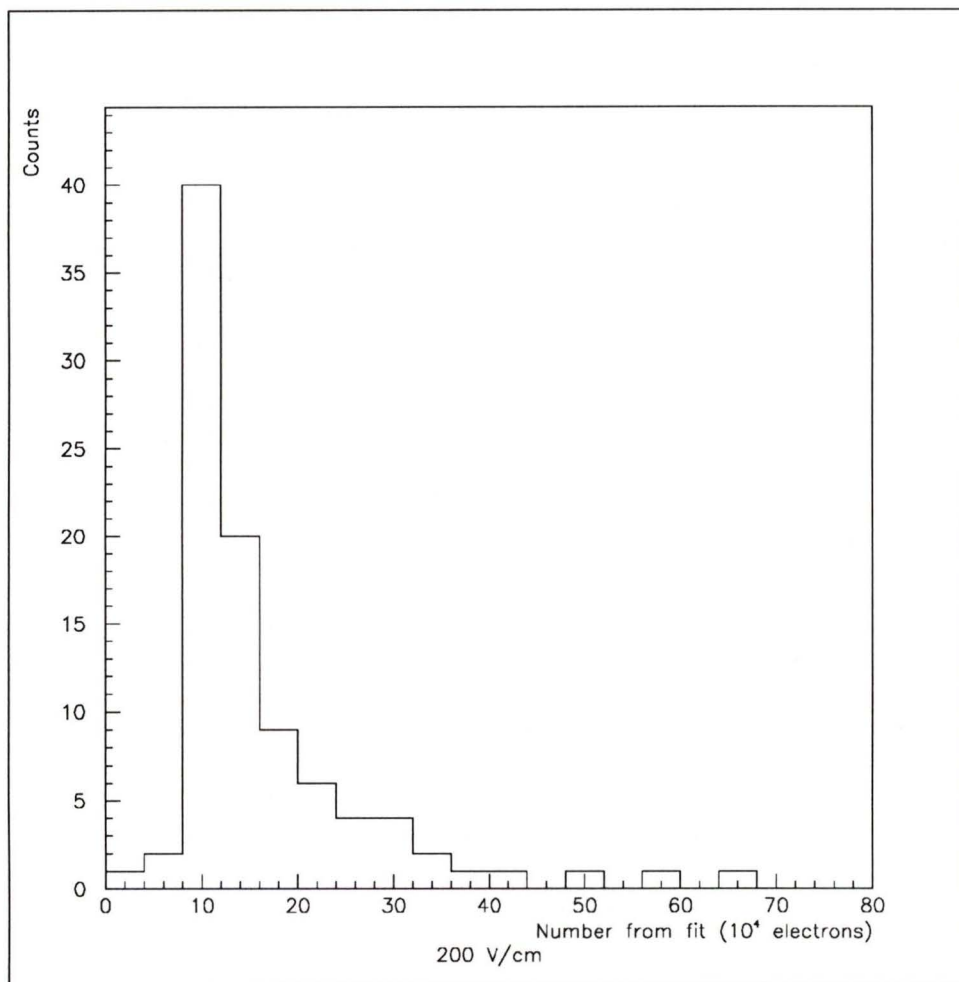


Figure 36: A typical free electron yield spectrum.

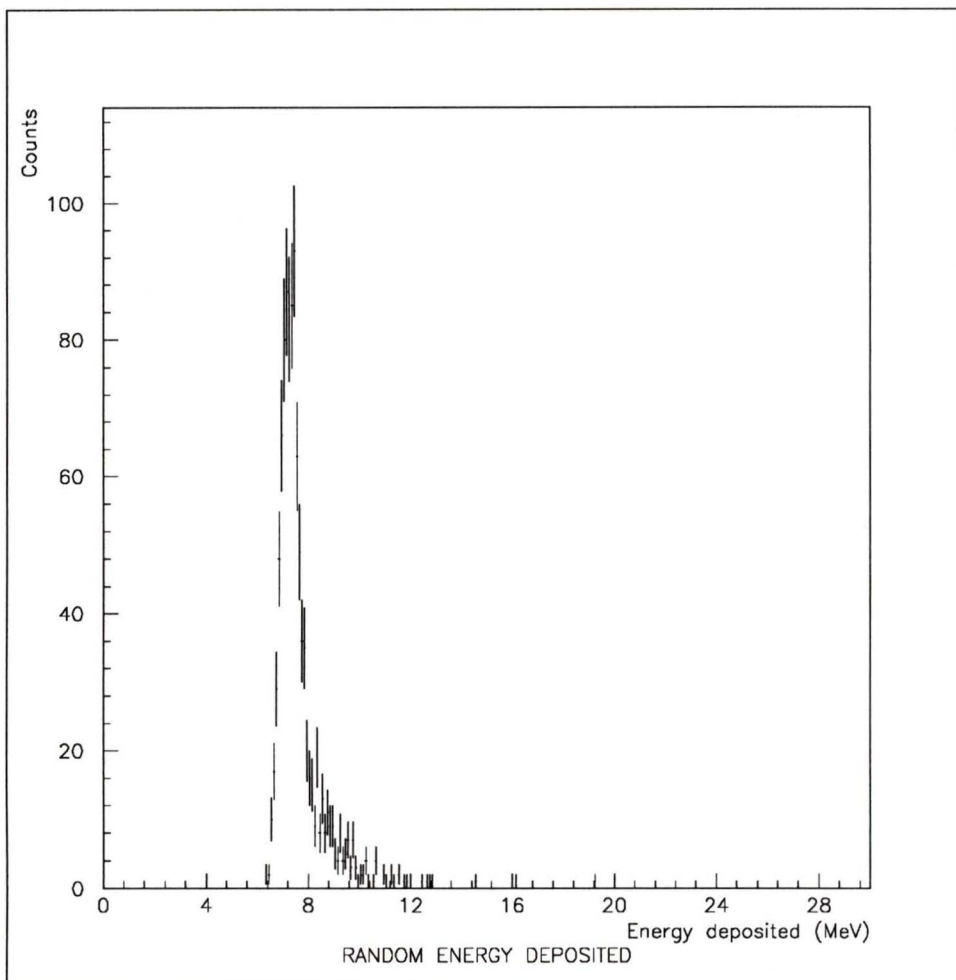


Figure 37: The random energy deposited in the cell.

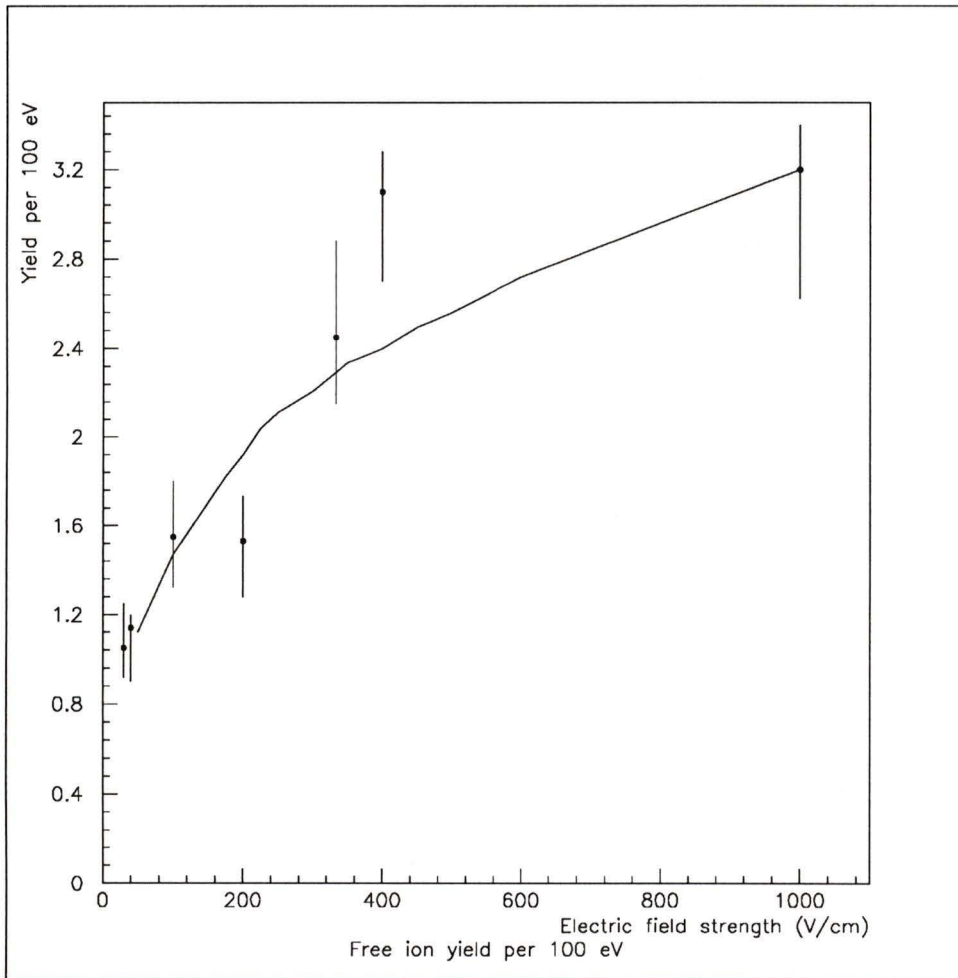


Figure 38: The free ion yield per 100 eV in our LAr sample. The line is from the data of reference [23].

5 Conclusion

We have succeeded in producing pure LAr and measuring the purity using pulse shape analysis. Our measured electron lifetime of $(95.2^{+7.1}_{-6.9} \pm 43)\mu s$ corresponds to an impurity level of 2.36 *ppb* O_2 equivalent, at an applied field of $30V/cm$. We find the low field electron mobility in our LAr to be $\mu_e = (451 \pm 1 \pm 68)cm^2/Vs$ with the mobility falling below this value at higher applied fields. This value agrees quite well with the accepted value of $460cm^2/Vs$ at $90K$ [9]. Finally our electron yield as a function of voltage demonstrates the same voltage dependence as that reported by Doe's group [23]. We found our free electron yield per 100eV at $1kV/cm$ applied field to be $3.2^{+0.2}_{-0.6}$, in excellent agreement with the 3.16 reported elsewhere [24].

We conclude that pulse shape analysis is an effective method in studying liquid properties, as it makes possible the simultaneous measurement of the electron mobility, the liquid purity and the free ion yield. Through this method we are able to identify the systematic effects arising from an incomplete knowledge of the readout electronics and estimate their magnitudes. This would not be the case if we were to look only at the pulse height, as the pulse height is a complicated function of the mobility, lifetime, yield and electronics response.

References

- [1] W.J. Willis and V. Radeka, Nucl. Instr. and Meth. 120(1974)221
- [2] S.E. Derenzo et. al. , Phys. Rev. A9(1974)2582
- [3] T. Doke, Portugal Phys. 12(1981)9
- [4] E. Buckley et. al. , Nucl. Instr. and Meth. A275(1989)364
- [5] L. Onsager, Phys. Rev. 54(1938)554
- [6] W. Hofmann et. al., Nucl. Instr. and Meth. 135(1976)151
- [7] George Bakale, Ulrich Sowada and Werner F. Schmidt, J. Phys. Chem. 80(1976)2556
- [8] A.O. Allen, NSRDS-NBS 58
- [9] Eido Shibamura et. al., Nucl. Instr. and Meth. 131(1975)249
- [10] G.N. Fowler and A.W. Wolfendale, in *Encyclopedia of Physics Vol XLVI/1*, S. Flügge ed. Springer-Verlag, Berlin(1961)
- [11] M. Aguilar-Benitez, et. al. , Phys. Lett. 170B(1986)43
- [12] W.R. Leo, *Techniques for Nuclear and Particle Physics Experiments* , Springer-Verlag, Berlin(1987)
- [13] L. Landau, J. Phys. 8(1944)201
- [14] P.V. Vavilov, Soviet Physics JETP 5(1957)749

- [15] B. Schorr, Computer Physics Communications 7(1974)215
- [16] Peter J. Doe et. al., Nucl. Instr. and Meth. A258(1987)170
- [17] Paul Horowitz and Winfield Hill ,*The Art of Electronics*, Cambridge University Press,Cambridge(1987)
- [18] A.B. Gillespie, *Signal, Noise and Resolution in Nuclear Counter Amplifiers*, Pergamon Press, New York(1953)
- [19] Linde Adsorbents, Union Carbide Corporation
- [20] Linde Specialty Gas, Prepurified Argon. Purity 99.9998% ($< 0.2\text{ppm } O_2$)
- [21] Centorr Model 2B-20-Q
- [22] MINUIT 'Function Minimization and Error Analysis', CERN Program Library
- [23] P.J. Doe et. al, IEEE Trans. Nucl. Sci. NS-29(1982)345
- [24] J-P. Dodelet et. al., Can. J. Chem 50(1972)1617

A Transfer function and Pulse shape

The effect any linear system has on its input can be calculated if one knows the response of the system to an impulse $\delta(t)$. This response is known as the transfer function $h(t)$ of the linear system. Given $h(t)$ for a system, the output $V_0(t)$ due to any other input $I(t)$ is given by,

$$V_0(t) = \int_0^t h(t-x)I(x)dx \quad (44)$$

here we note by convention that

$$h(t) = 0 \quad t < 0 \quad (45)$$

The transfer functions for simple RC integrators and differentiators are easily obtained to be

$$h_{int}(t) = 1/\tau e^{-t/\tau} \quad (46)$$

and

$$h_{diff}(t) = \delta(t) - 1/\tau e^{-t/\tau} \quad (47)$$

In (46) and (47) $\tau \equiv RC$, the time constant of the circuit.

In the electronics chain considered there are basically two integrators and two differentiators (see figure 39). We note that to find the transfer function of the entire circuit, we must do three convolution integrals. The impulse response at AA' is just

$$V_{AA'} = \frac{1}{\tau_1} e^{-\frac{t}{\tau_1}} \quad (48)$$

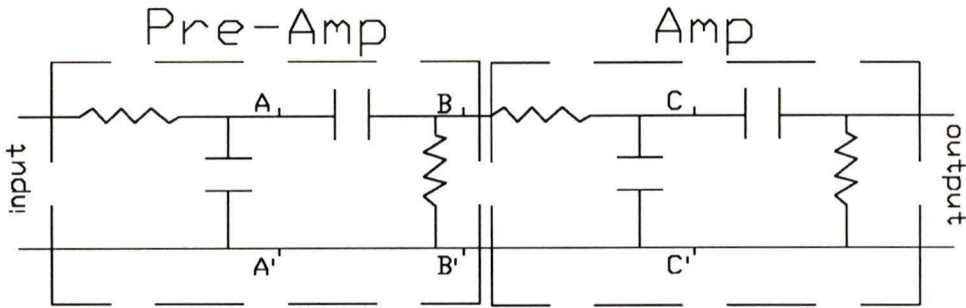


Figure 39: The equivalent circuit for an amplification chain.

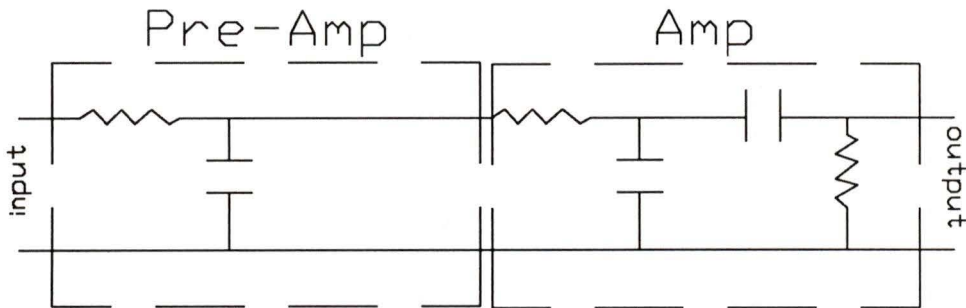


Figure 40: The pre-amp approximated by a single integrator.

thus at BB' the voltage due to an impulse at the input is

$$V_{BB'}(t) = \int_0^t V_{AA'}(t-x) \left[\delta(x) - 1/\tau_2 e^{-x/\tau_2} \right] dx \quad (49)$$

and so on for the entire circuit.

For most pre-amps τ_2 is much larger than the time scales to be considered. This being the case, we replace figure (39) by figure (40), i.e.: let $\tau_2 \rightarrow \infty$ in (47). With this approximation the transfer function of the electronics chain can be written

$$h(t) = \begin{cases} 0 & t < 0 \\ A [e^{-t/\tau_1} - e^{-t/\tau_2}] + B [e^{-t/\tau_1} - e^{-t/\tau_3}] + C [e^{-t/\tau_2} - e^{-t/\tau_3}] & t > 0 \end{cases} \quad (50)$$

The constants A, B and C depend on the various time constants and also take into account the amplification of the system.

Thus the expected signal out of the amplification system, resulting from the input signal given in equation (18) is:

$$V_0(t) = \begin{cases} 0 & t < 0 \\ [A + B]c(\tau_1) + [C - A]c(\tau_2) - [B + C]c(\tau_3) & 0 \leq t \leq \tau_d \\ [A + B]\gamma(\tau_1) + [C - A]\gamma(\tau_2) - [B + C]\gamma(\tau_3) & t > \tau_d \end{cases} \quad (51)$$

where

$$\begin{aligned} c(\tau_1) &= \frac{1}{a} \left\{ e^{-t/\tau} - e^{-t/\tau_1} - \frac{1}{a\tau_d} \left[e^{-t/\tau}(at - 1) + e^{-t/\tau_1} \right] \right\} \\ a &\equiv \left(\frac{1}{\tau_1} - \frac{1}{\tau} \right) \end{aligned} \quad (52)$$

and

$$\gamma(\tau_1) = \frac{e^{-t/\tau_1}}{a} \left[\frac{1}{a\tau_d} (e^{a\tau_d} - 1) - 1 \right] \quad (53)$$

VITA

Surname: Schenk
Place of Birth:
Date of Birth:

Given Names: Paul Robert
Niagara on the Lake, Ontario
June 5, 1965

Educational Institutions Attended:

Champlain Regional College, Lennoxville	1982
Vanier College, St. Laurent	1983
Champlain Regional College, Lennoxville	1984
University of Western Ontario, London	1984 to 1987
University of Victoria, B.C.	1987 to 1989

Degrees Awarded:

Diplôme d'études collégiales	1984	Champlain Regional College, Lennoxville
B.Sc. (Honors)	1987	University of Western Ontario, London

Honours and Awards:

NSERC Postgraduate Scholarship	1987 to 1989
President's Research Scholarship	1987 to 1989
MacDonnell Graduate Award in Physics	1987 to 1988
R.M. Pearce Memorial Fellowship	1988 to 1989

PARTIAL COPYRIGHT LICENSE

I hereby grant the right to lend my thesis (the title of which is shown below) to users of the University of Victoria Library, and to make single copies only for such users or in response to a request from the Library of any other university or similar institution, on its behalf or for one of its users. I further agree that permission for extensive copying of this dissertation for scholarly purposes may be granted by me or a member of the University designated by me. It is understood that copying or publication of this thesis for financial gain shall not be allowed without my written permission.

Title of Thesis:

Transient Analysis of Electrons Drifting in Liquid Argon



April 3, 1989

April 3, 1989



National Library
of Canada

Bibliothèque nationale
du Canada

Canadian Theses Service Service des thèses canadiennes

Ottawa, Canada
K1A 0N4

The author has granted an irrevocable non-exclusive licence allowing the National Library of Canada to reproduce, loan, distribute or sell copies of his/her thesis by any means and in any form or format, making this thesis available to interested persons.

The author retains ownership of the copyright in his/her thesis. Neither the thesis nor substantial extracts from it may be printed or otherwise reproduced without his/her permission.

L'auteur a accordé une licence irrévocable et non exclusive permettant à la Bibliothèque nationale du Canada de reproduire, prêter, distribuer ou vendre des copies de sa thèse de quelque manière et sous quelque forme que ce soit pour mettre des exemplaires de cette thèse à la disposition des personnes intéressées.

L'auteur conserve la propriété du droit d'auteur qui protège sa thèse. Ni la thèse ni des extraits substantiels de celle-ci ne doivent être imprimés ou autrement reproduits sans son autorisation.

ISBN 0-315-50114-6